Experimental investigation and DEM-CFD analysis of Darcy–Forchheimer flows in randomly packed bed systems of wood particles

Shaolin Liu [a,b], Azita Ahmadi-Senichault [a,b], Amine Ben-Abdelwahed [a,b], Hui Yao [b,c,*], Jean Lachaud [b,c]

[a] Arts et Métiers Institute of Technology, 33400, Talence, France
[b] I2M - Institute of Mechanical Engineering of Bordeaux: UMR CNRS 5295, University of Bordeaux, Arts et Métiers Institute of Technology, Hesam Université, Bordeaux INP, INRAE, 33400, Talence, France
[c] Univ. Bordeaux, 33400, Talence, France

ARTICLE INFO

ABSTRACT

Understanding the packing structure and pressure drop across a randomly packed bed of wood particles is essential for the design and control of wood drying, pyrolysis, and gasification processes. This study utilizes experimental and micro-scale simulation methods to explore fluid dynamics within packed bed systems of wood particles and glass spheres. Pressure drop and velocity data from experiments and simulations were fitted using Darcy's law and the Darcy–Forchheimer law to derive key parameters: permeability (K) and Forchheimer coefficient (β), which were then compared with existing correlations. Experiments were conducted in packed beds of wood pellets (Re = 11.5 to 185.1) and glass spheres (Re = 28.3 to 455.7). The Discrete Element Method (DEM) was used to generate packed bed structures of cylindrical and spherical particles, corresponding to the experiments. Flow within the beds was modeled using the incompressible Navier–Stokes equations, with detailed analyses of streamlines and vorticity. CFD results indicated critical Reynolds numbers of 10.1 for glass spheres and 4.1 for wood pellets, marking the transition from Darcy to Forchheimer flow regimes. Beyond these values, the formation of vortices indicated nonlinear effects. Experiments showed that K values were 2.95×10^{-7} m^2 and β values 1.22×10^3 m^{-1} for glass spheres; and for wood pellets, K values were 9.82×10^{-8} m^2 and β values 3.04×10^3 m^{-1}. Using experimental results as references, simulation errors were lower than those from the correlations. Specifically, for wood pellets, simulation errors were 13.54% for K and 10.20% for β, while correlation errors were 42.57% for K and 7.89% for β. This indicates that simulation results are more reliable than existing correlations.

1. Introduction

Fuel wood packed bed systems are increasingly utilized in renewable energy recovery and conversion technologies such as drying [1], pyrolysis [2,3], and combustion or gasification [4]. These systems typically consist of cylindrical vessels filled with various particles like wood spheres [5], pellets [6], or chips [7], forming porous media. Understanding the diverse flow states and associated pressure drops in these porous media is essential for optimizing their practical applications, as the gas flow can affect heat transfer [8,9], chemical reaction rates, and the composition of the resulting products. Gas flow through packed beds can be modeled on macro or micro scales respectively [10,11]. Micro-scale models account for the heterogeneity of pores and fluid–solid interaction [12,13], while macro-scale models treat the packed bed as a homogeneous and isotropic medium, describing transport

phenomena through averaged governing equations [14,15]. Micro- and macro-scales can be linked through an upscaling method such as the homogenization theory [16] or the volume-averaging techniques [17], which are the most popular methods in the context of packed beds.

Flow regimes in porous media can be broadly classified into the Darcy (creeping) regime, Forchheimer (inertial) regime, and turbulent regime [18–20]. Sedghi-Asl et al. [19] measured flow in porous rockfill media and identified three flow regimes: linear Darcy for Reynolds numbers below 120, transitional for 120 to 10,000, and turbulent for above 10,000, using the average particle diameter to calculate Reynolds numbers. Zeng et al. [20] used the Reynolds number and Forchheimer number ($Fo = (K\beta\rho_g\langle v_g\rangle)/\mu_g$) to identify non-Darcy flow onset in nitrogen flow through sandstone, finding a critical Forchheimer number of 0.11. Bağcı et al. [18] identified flow regimes from Darcy to turbulent in

---

Nomenclature

Acronyms

CFD	computational fluid dynamics
DEM	discrete element method
FEM	finite element method
FVM	finite volume method
LBM	lattice Boltzmann method
REV	representative elementary volume
XCT	X-ray computed tomography

Greek symbols

β	Forchheimer coefficient, m^{-1}
ε_A	radial porosity of the packed beds
ε_g	porosity
μ_g	dynamic viscosity of gas, $\mathrm{kg\,m^{-1}\,s^{-1}}$
ξ	modification factor
ρ_i	density of the i-phase, $\mathrm{kg\,m^{-3}}$
τ	tortuosity
Φ	correction factor
$\boldsymbol{\omega}$	vorticity vector, s^{-1}

Latin symbols

A	area, m^2
B_W	wall correction term
d_c	cylinder diameter, m
d_{eq}	equivalent diameter, m
d_s	sphere diameter, m
D	tube inner diameter, m
f	dimensionless pressure drop
Fo	Forchheimer number
K	permeability, m^2
K_{eff}	effective permeability, m^2
l	dimensionless distance from the wall
l_c	the average length of wood pellets, m
L	packed beds length, m
M	gas molar mass, $\mathrm{kg\,mol^{-1}}$
ΔP	pressure drop used in the experiment, $\mathrm{kg\,m^{-1}\,s^{-2}}$
P	gas pressure used in the experiment, $\mathrm{kg\,m^{-1}\,s^{-2}}$
p	gas pressure, $\mathrm{kg\,m^{-1}\,s^{-2}}$
$\langle p_g \rangle^g$	intrinsic average pressure, $\mathrm{kg\,m^{-1}\,s^{-2}}$
$\Delta \langle p_g \rangle^g$	intrinsic average pressure drop, $\mathrm{kg\,m^{-1}\,s^{-2}}$
$\nabla \langle p_g \rangle^g$	intrinsic average pressure gradient, $\mathrm{kg\,m^{-2}\,s^{-2}}$
qm	gas mass-flow rate, $\mathrm{kg\,s^{-1}}$
qv	gas volume-flow rate, $\mathrm{m^3\,s^{-1}}$
R	gas constant, $\mathrm{J\,K^{-1}\,mol^{-1}}$
Re	Reynolds number
Re_p	particle Reynolds number, $Re/(1-\varepsilon_g)$
S	single cylinder surface area, m^2
$\mathbf{v_g}$	velocity of the gas phase, $\mathrm{m\,s^{-1}}$
$\langle \mathbf{v_g} \rangle^g$	intrinsic phase average velocity of the gas, $\mathrm{m\,s^{-1}}$
$\langle \mathbf{v_g} \rangle$	superficial average velocity, $\mathrm{m\,s^{-1}}$
V	averaging volume, m^3
V_c	single cylinder volume, m^3

Subscripts

eff	effective
g	gas
in	inlet
out	outlet
s	solid

packed beds of spheres, including transitional regimes. They suggested using the square root of Darcy-regime permeability as the length scale in the Reynolds number. Kundu et al. [21] conducted experimental and numerical studies on fluid flow in a packed bed of glass particles and observed three main flow regimes: Darcy, and non-Darcy, along with two transition regimes (transition to Darcy and weak inertia flow). Flow regimes in packed beds of fuel wood particles are rarely studied, especially in terms of visualizing microscopic flow behavior.

Structural parameters, porosity ε_g and radial porosity ε_A can reflect the structure of the bed to a certain extent [6,22]. Both ε_g and ε_A are influenced by particle size, shape, and the packing method, with detailed influencing factors available in a relevant review [23]. Various experimental, simulation, and theoretical studies have investigated the structure inside packed beds [5,24,25]. Experimental methods include slicing on a lathe [26], radiography [27], magnetic resonance imaging (MRI) [28], fluorescence [29], and X-ray tomography [30]. X-ray tomography can provide high-resolution 3D images but requires specialized and expensive equipment. It also has limitations such as long scanning times, and limited sample sizes for large samples, making it unsuitable for studying large packed beds and large numbers of samples. Simulation studies primarily rely on the Discrete Element Method (DEM), which is widely recognized as a powerful and reliable tool for studying the structure of packed beds. Combining Computational Fluid Dynamics (CFD) with DEM represents an advanced approach in numerical modeling [7,31]. Theoretical methods are based on geometric and analytical techniques, using arc length to calculate the radial porosity profile at any given axial position or the total axial position [27]. Porosity profiles and radial porosity curves for different spherical particle-to-tube ratios, based on the aforementioned methods, are well-documented in numerous studies [24,25,30,32], showing that the radial porosity curve exhibits an oscillating pattern in packed beds of uniform spheres. In contrast, determining porosity in packed beds with non-spherical or irregularly shaped particles, particularly wood pellets, is less well-studied. Hamel et al. [6] analyzed images of solidified packing slices to determine radial porosity variation in packed beds of wood pellets and proposed a mathematical expression. They found that the radial porosity distribution depends on the core porosity and the dimensionless distance from the tube wall. Pozzobon et al. [7] used LMGC90, a DEM code, to generate a packed bed of wood chips and analyzed the overall porosity. Their work paves the way for the numerical estimation and analysis of structural parameters in packed beds.

In macroscopic models, besides porosity ε_g, flow characteristics like permeability K and the Forchheimer coefficient β need to be determined. To estimate K and β, correlations such as the Ergun or Kozeny-Carman expressions are widely adopted for packed beds of spherical particles [33], and adapted for irregular particles [34]. For more general geometries, determinations start by obtaining a steady-state pressure drop data of a flow in pack beds, by experiments [18,34,35] or micro-scale simulations [5,7,36–38], and then apply equations such as Darcy's, the extended Brinkman–Darcy, or Darcy–Forchheimer to calculate coefficients. Each equation has its applicable flow ranges. In the experimental method, to measure the pressure drop under steady-state conditions, it is required to have a fluid with known viscosity traverse a bed at well-controlled mass flow rates [22,34,39]. But it is often difficult to achieve ideal experimental conditions, especially for smaller pressure drops [40]. In the simulation methods [10], the structure of a packed bed can be either obtained by scanning a real packed

Table 1
Summary of the values of K and β found in the literature.

Investigators	Media	Method	Equivalent diameter	Darcy velocity	Results	
			d_{eq} (mm)	$|\langle v_g \rangle|$ (m/s)	K (m^2)	β (m^{-1})
Yazdanpanah et al. [22]	wood pellet	Experimental	4–32	0.014–0.8	5.63×10^{-8}	2.79×10^3
			6.7–10		6.37×10^{-8}	2.25×10^3
			4–6		2.55×10^{-8}	3.14×10^3
Victor et al. [7]	wood chips	Experimental	2-4.5	0.005–0.05	1.63×10^{-8}	
		Numerical		0.0005–5.0	1.89×10^{-8}	
Mayerhofer et al. [34]	wood chips	Experimental	8.7	0.05–0.8	1.30×10^{-7}	1.37×10^3
			5.5		7.8×10^{-8}	1.70×10^3
			2.4		1.5×10^{-8}	4.35×10^3

bed with X-ray computed tomography (XCT) [41] or generated by the discrete element method (DEM) [7,36,42]. DEM is widely used to simulate the flow dynamics of granular materials by applying Newton's second law to individual particles. Jiang et al. [43,44] employed DEM with LIGGGHTS software to model the geometric structure of randomly packed beds and examine turbulent flow characteristics and vortex behaviors under various conditions. Their work showed that complex turbulent eddies form within the packed bed pores, with large eddies mainly found at the main channel entrance and near the spherical wall. Das et al. [45] also utilized DEM with LIGGGHTS to develop a model for flow through cylindrical fixed-bed reactors with randomly packed porous non-spherical particles. They further proposed a relationship between the dimensionless pressure drop (f) and the Reynolds number (Re), expressed as $f = a + bRe^{0.68}$. Džiugys et al. [29] used DEM simulations to investigate the relationship between the smallest particle diameter in a packed bed and its porosity. Their findings revealed that the relationship between bed porosity and the smallest particle size can be accurately described by a fractal law. After constructing the mesh in the void of the packed bed, the Navier–Stokes equations are solved to determine the steady-state pressure drop. This value is then averaged over the domain to obtain the macro-scale pressure drop [10]. Numerous correlations for calculating pressure drop due to fluid flow through packed beds have been presented in the literature, as summarized by Erdim et al. [46]. Experiments were conducted with water flowing through packed beds of glass spheres of various sizes, and the results were compared with 38 correlations from the literature. It was found that, although the Ergun equation is the most widely used, it should not be applied to particle Reynolds number ($Re_p = Re/(1-\varepsilon_g)$) above 500. A new, simpler equation ($f = 160 + 2.81 Re_p^{0.904}$) was proposed to represent the data collected. This study focuses on the pressure drop in packed beds composed of wood. A summary of the values of K and β and their application ranges is presented in Table 1. The dataset indicates that K and β values vary with particle size. This variability introduces uncertainty in the applicability of existing data to wood pellets.

The objective of this work is to identify each flow regime in terms of a critical Reynolds number, determine macroscopic properties: permeability and the Forchheimer coefficient, and obtain structural parameters like porosity and radial porosity of particles within the packed bed through experimental and DEM-generated structure-based characterization. For this purpose, fluid flow within a packed bed of glass beads and cylindrical wood pellets is studied experimentally. The Reynolds numbers range from 28.3 to 455.7 for glass spheres and 11.5 to 185.1 for wood pellets, representing biomass gasification applications. Two kinds of 3D randomly packed beds filled with particles of the same shape and material properties as those used in the experiments are generated via the DEM software LIGGGHTS. Structural parameters like porosity and radial porosity, which are not easy to measure directly through experiments, are analyzed. An incompressible flow under constant temperature, characterized by the incompressible Navier–Stokes equations, is solved in this packed bed. The solutions are then used to obtain permeability and the Forchheimer coefficient. A detailed analysis of the flow behavior, including streamlines and vorticity, was conducted based on the micro-scale simulation results.
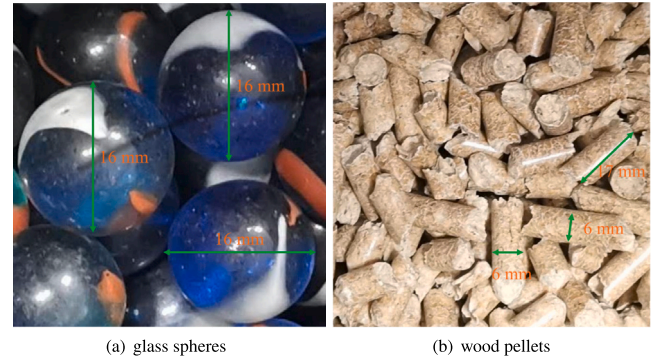

(a) glass spheres   (b) wood pellets

Fig. 1. Photograph of the two types of particles used in the experiment.

The article is structured as follows: Section 2 outlines the experimental setup, and test procedure, and presents experimental results related to pressure drop in packed bed made of glass spheres and wood pellets. Section 3 involves the reproduction of sphere and cylinder packed beds by DEM, followed by CFD micro-scale simulation. In Section 4, numerical results and estimated values of permeability and the Forchheimer coefficient are discussed. Section 5 provides a concise conclusion.

2. Materials and method

The experiment aims to estimate the permeability and Forchheimer coefficient by measuring flow rates and pressure drops in a packed bed. In the first subsection, the materials used in this work are introduced. In the next three subsections, the experimental system and test procedure are presented, followed by the analysis of measurement data for packed beds of glass spheres and wood pellets.

2.1. Material

In this paper, two types of particles were used in the experiment: glass spheres and wood pellets. The glass spheres were uniform with a diameter d_s of 16 mm, while the wood pellets had a diameter d_c of 6 mm and lengths ranging from 3 to 27 mm, as shown in Fig. 1.

Fig. 2 shows the length distribution of 500 measured wood pellets used in the experiments. Most pellets have lengths between 7 mm and 12 mm, with peaks around 8 mm and 11 mm. The monomodal distribution indicates a single prominent length range, with an average pellet length of 8 mm and a standard deviation of 0.8 mm. The equivalent diameter of the wood pellets, d_{eq}, is defined as the Sauter mean diameter as follows [7]:

$$d_{eq} = \frac{6V_c}{S} = \frac{6\pi(d_c/2)^2 l_c}{\pi d_c l_c + 2\pi(d_c/2)^2} = \frac{6 d_c l_c}{4 l_c + 2 d_c} = 6.5 \text{ mm} \qquad (1)$$

where V_c and S are the volume and surface area of the wood pellet, based on the average length l_c.
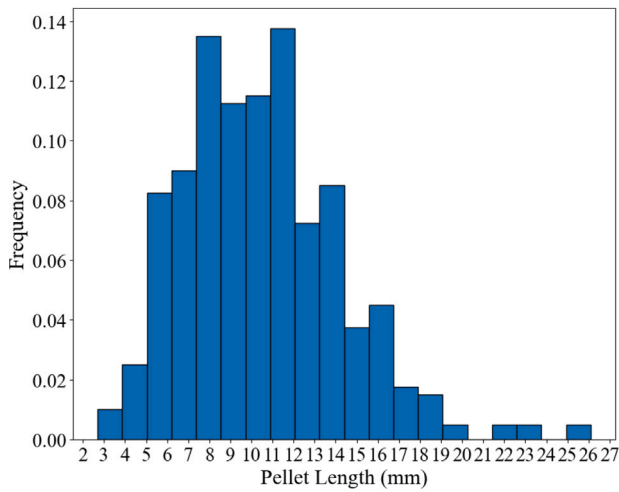
Fig. 2. Length distribution of 500 measured wood pellets used in the experiments.

Table 2
Properties of the two types of particles and air.

Properties	Symbol	Glass spheres	Wood pellets	Air
Equivalent diameter	mm	16	6.5	-
Moisture content	–	–	6.2	–
Density	$kg\,m^{-3}$	2500	1200	1.2
Viscosity	$kg\,m^{-1}\,s^{-1}$	–	–	1.9×10^{-5}

The physical parameters of the two types of particles (glass spheres and wood pellets) and the gas (air) used in the experiment are presented in Table 2. The moisture content of the wood pellets, measured with a moisture analyzer (METTLER TOLEDO, HC103), is 6.2%. The physical properties of the air are based on data at room temperature (T = 293 K) [8].

2.2. Experiment setup and procedure

Figs. 3 and 4 respectively show the schematic diagram and photographic view of the experimental setup for measuring the pressure drop across a packed bed filled with different types of particles. The system was designed and installed at the I2M, Institute of Mechanics and Engineering, University of Bordeaux.

The system is divided into three parts: the flow control subsystem, the packed bed subsystem, and the data acquisition subsystem. The flow control subsystem includes an air blower (BAK Thermoplastic) to supply air at controlled rates. The packed bed subsystem consists of an iron tube and two metallic grids to maintain the spherical or cylindrical particles. The data acquisition subsystem includes a differential pressure transmitter (EMERSON FISHER ROSEMOUNT) to measure pressure drop and a flow meter (VT 110-2014 THERMO-ANEMOMETER) to measure gas velocity. The iron tube has dimensions

of 940 mm in length, 194 mm in inner diameter, and a thickness of 3 mm [8]. This setup enables investigations of pressure variations across a packed bed under controlled conditions, with verified air-tight integrity before and after measurements

The flow rate of the inlet gas is controlled by the air blower and measured using a flow meter. The range of air volume-flow rate (qv) is from 50 to 800 L/min. At room temperature, this corresponds to an air mass-flow rate (qm) ranging from 0.001 to 0.016 kg/s ($qm = qv \cdot \rho_g$ with $\rho_g = 1.20$ kg/m³). The Darcy velocity ($\langle v_g \rangle$) within the packed beds was from 0.028 to 0.451 m/s ($\langle v_g \rangle = 4qv/(\pi \cdot D^2)$), where D is the inner diameter of the tube, 0.197 m). The Reynolds number based on the equivalent diameter is defined as follows:

$$Re = \rho_g |\langle v_g \rangle| d_{eq}/\mu_g \tag{2}$$

The values of each parameter used in Eq. (2) are listed in Table 2. Based on Eq. (2), the Reynolds numbers range from 28.3 to 455.7 for glass spheres and from 11.5 to 185.1 for wood pellets. In summary, the ranges of these parameters are presented in Table 3.

To capture the pressure drop across the packed bed, a differential pressure transmitter with a range of 0 to 620 mbar (0 to 62000 Pa) was used [47]. The transmitter's electrical signals, accurate to 0.0001 (6.2 Pa), were relayed to a data acquisition system for real-time observation and analysis. Fluid velocity was measured using a flowmeter with a range of 0.15 to 30 m/s, corresponding to velocities within the packed bed from 0.012 to 2.411 m/s, with an uncertainty of ±1% of the reading. Each experiment was repeated following a consistent procedure to ensure data reproducibility.

2.3. Data analysis

The one-dimensional flow of air through the packed bed is described by Darcy's law and the Forchheimer equation given respectively as [21, 47]:

$$\frac{\Delta P}{L} = \frac{\mu_g}{K} \cdot |\langle v_g \rangle| = \frac{\mu_g^2}{K \rho_g d_{eq}} Re \tag{3}$$

$$\frac{\Delta P}{L} = \frac{\mu_g}{K} \cdot |\langle v_g \rangle| + \rho_g \beta |\langle v_g \rangle|^2 = \frac{\mu_g^2}{K \rho_g d_{eq}} Re + \frac{\beta \mu_g^2}{\rho_g d_{eq}^2} Re^2 \tag{4}$$

where ΔP is the pressure drop measured by the differential pressure transmitter, L is the length of the tube, K is the permeability, and β is the Forchheimer coefficient.

For glass spheres with uniform diameters, Eq. (3) is applicable when the Reynolds number (Eq. (2)) is less than 10 [48]. For higher Reynolds numbers (Re > 10), Eq. (4) is needed to describe the relationship between pressure drop and Darcy velocity. However, for wood pellets with uneven length distribution, the critical value of the Reynolds number between Eqs. (3) and (4) needs to be determined.

The data analysis method begins by defining an effective permeability K_{eff} as specified in Eq. (5).

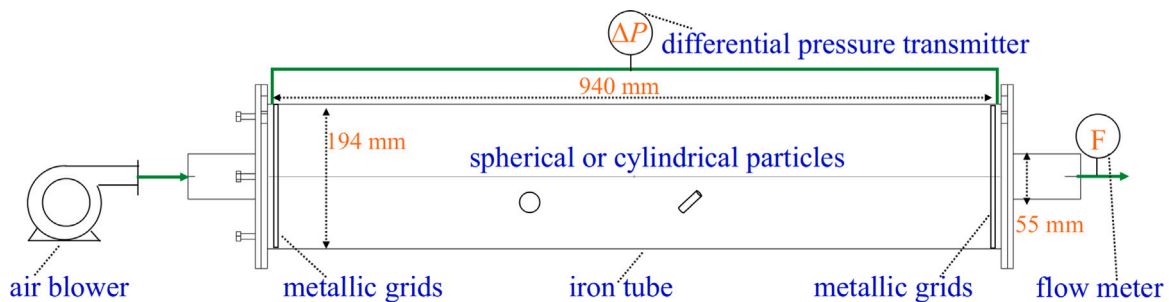$$K_{eff} = \frac{\mu_g^2}{\rho_g d_{eq}} \frac{L}{\Delta P} Re \tag{5}$$

Fig. 3. Schematic diagram of the experimental setup.

Fig. 4. Photographic view of the experimental setup with some detailed images.

Table 3
Ranges of experimental parameters.

Parameters	Air volume-flow rate	Air mass-flow rate	Darcy velocity	Reynolds number	
Symbol	qv (L min^{-1}) or (m^3 s^{-1})	qm (kg s^{-1})	$\langle v_g \rangle$ (m s^{-1})	Re (glass spheres)	Re (wood pellets)
Definition		$qv \cdot \rho_g$	$4qv/(\pi \cdot D^2)$	$\rho_g |\langle v_g \rangle| d_{eq}/\mu_g$	$\rho_g |\langle v_g \rangle| d_{eq}/\mu_g$
Minimum	50 or 0.000833	0.001	0.028	28.3	11.5
Maximum	800 or 0.013333	0.016	0.451	455.7	185.1

Within the Darcy regime, K_{eff} remains constant and represents the permeability K we seek. In the Forchheimer regime, K_{eff} includes both the permeability K and a term involving the Forchheimer coefficient β. This approach helps us achieve two goals: determining the critical Reynolds number that separates the two flow regimes, and finding the permeability K in the Darcy regime and the Forchheimer coefficient β in the Forchheimer regime by fitting the data to Eqs. (3) and (4), respectively.

2.4. Experimental results

During the experiment, each measurement of pressure difference was taken three times for each of the ten different mass-flow rates (qm). The observed deviation was not larger than 6.2 Pa. Therefore, only the averaged values are reported here.

The relationship between measured pressure gradient $\Delta P/L$ and Reynolds number Re for packed beds of both glass spheres and wood pellets is plotted in Fig. 5(a), where Re is computed following Eq. (2). The error in Fig. 5(a) is ±6.6 Pa/m, which is attributed to the measurement accuracy of the differential pressure transmitter. However, due to the small size of the error bars, they are difficult to observe in the image, as they fall within the boundaries of the square or circular markers. It is observed that the pressure gradient displays a nonlinear increase with the increment of the Reynolds number, which confirms the flow within the Forchheimer regime. This observation is further supported by Fig. 5(b), where K_{eff} (defined in Eq. (5)) is not constant and gradually decreases with increasing Re, indicating that our experiment only includes the Forchheimer regime and not the Darcy flow regime. This is due to the difficulty of the differential pressure transmitter in

measuring the smaller pressure differences associated with the lower Reynolds numbers in the Darcy regime. Additionally, Fig. 5 (b) shows that the effective permeability K_{eff} has greater uncertainties at lower Reynolds numbers, which is directly influenced by the measurement accuracy limitations at these lower values.

To obtain the values of K and β, Eq. (4) was used to fit the relationship between $\Delta P/L$ and Re. Fig. 5(a) shows the fitted curves as green and red solid lines. The R^2 values indicate the accuracy of the fit, allowing for the extraction of parameter values from the fitted coefficients. The values for both K and β are presented in Table 4. The table shows that glass spheres and wood pellets have permeability and Forchheimer coefficient values of the same order of magnitude. However, wood pellets have lower permeability and higher Forchheimer coefficient, indicating greater resistance to fluid flow. This is due to their irregular shape and size, causing a more complex flow path and higher friction losses. Except for the experimental methods to determine K and β, the analysis and comparison with determination by correlation and simulation methods will be covered in Section 4.1, where all three methods will be compared and discussed.

A brief summary is provided to highlight the potential limitations of the experimental work. The study focused on spherical particles and cylindrical wood pellets, without testing other material types, which may limit the applicability of the findings to other particle shapes or compositions. Additionally, the experiments were conducted under specific conditions, with a primary focus on flow behavior, and did not consider the effects of high-temperature gas heat transfer. As a result, the impact of thermal gradients and material properties under varying temperature conditions was not addressed, which could be important for applications involving elevated temperatures.
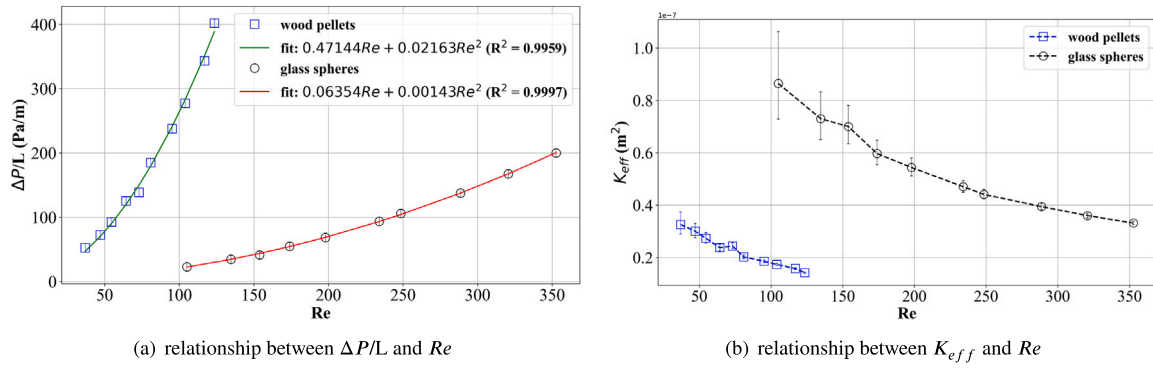
(a) relationship between $\Delta P/L$ and Re (b) relationship between K_{eff} and Re

Fig. 5. Measured pressure gradient and effective permeability with increasing Reynolds number.

(a) size of single particles (b) packing process of particles (c) 3D packed bed of particles
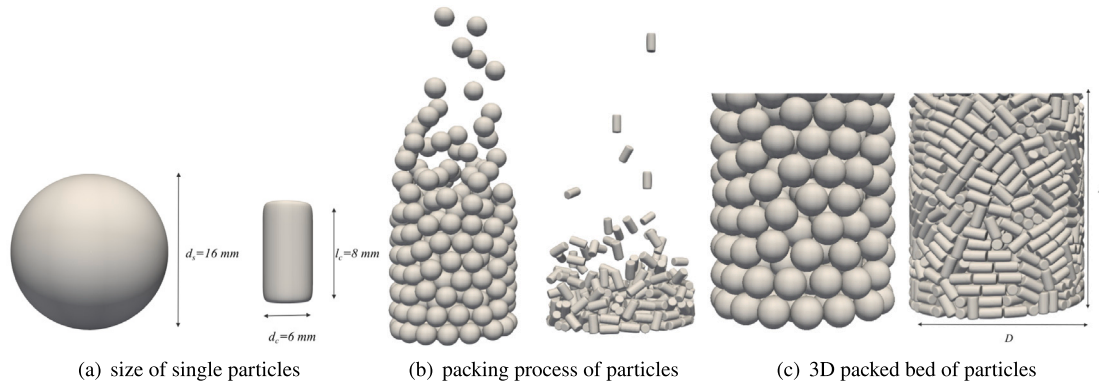
Fig. 6. Views of packed beds with spherical and cylindrical particles.

Table 4
Permeability K and Forchheimer coefficient β in packed beds filled with different particles.

Particles	Permeability, K (m^2)	Forchheimer coefficient, β (m^{-1})	Coefficient of determination R^2
Glass spheres	2.95×10^{-7}	1.22×10^3	0.9997
Wood pellets	9.82×10^{-8}	3.04×10^3	0.9959

3. Numerical approach

This section presents the process of using the DEM code to construct packed beds filled with particles of the same shape and material properties as those used in the experiments. The porosity and radial porosity distributions of both types of packed beds are analyzed. Fluid dynamics within these packed beds are simulated by solving the incompressible Navier–Stokes equations, as for Reynolds numbers ($Re < 1000$) and constant temperature conditions, the fluid is treated as incompressible [7,11,49]. The numerical solutions at the micro-scale are then averaged into the macro-scale for the determination of K and β.

3.1. Packed bed generation and analysis

3.1.1. Medium generation

To generate a geometric representation of randomly packed beds that accurately reflects their stacking structure, we employed the open-source software LIGGGHTS [11,50]. This software employs the DEM to model various shapes of particles, such as spheres and cylinders, falling into a virtual tube under gravity. All interactions, including collisions and rebounds between the particles and with the tube walls, are taken into account. To maintain consistency with the experiments, glass is used for spherical particles and wood for cylindrical particles. Their density and size information are defined in Table 2. Simulation parameters, including Young's modulus, Poisson's ratio, coefficient of

Table 5
Simulation parameters for generating the packed bed.

Parameter	Glass spheres	Wood pellets	Reference
Young's modulus (N m^{-2})	7.3×10^{10}	1.6×10^{10}	[51,52]
Poisson's ratio	0.228	0	[52,53]
Coefficient of restitution	0.9	0.76	[52]
Coefficient of friction	0.05	0.50	[52]

restitution, and surface roughness (represented by the coefficient of friction) [45], are detailed in Table 5.

The sizes of particles used in the simulations are displayed in Fig. 6(a). The sphere diameter is set at $d_s = 16$ mm. For cylindrical particles, the diameter (d_c) is fixed at 6 mm, with the length (l_c) standardized to the average observed in experiments at 8 mm, giving an equivalent diameter $d_{eq} = 6.5$ mm as defined in Eq. (1). Fig. 6(b) shows the packing process. Spherical or cylindrical particles are introduced at the top of the tube and descend to the flat surface at the bottom under the force of gravity. The software tracks each particle's trajectory and interactions with other particles and the domain walls, applying Newton's laws of translational and rotational motion. The packing process concludes when the particles' kinetic energy is fully dissipated, and they come to a complete stop. Fig. 6(c) provides a visualization of the fully formed packed beds. The tubes accommodating these particles maintain a constant length L of 200 mm for spheres, and 100 mm for cylinders, respectively. This difference is because the spheres have a diameter of 16 mm, while the equivalent diameter of the cylinders

Table 6

Size ratios of packed beds. The tube diameter D varies from 20 to 260 mm, with a sphere diameter d_s of 16 mm. For cylinders, the equivalent diameter d_{eq} is 6.5 mm, as in Eq. (1).

Case	1	2	3	4	5	6	7	8	9	10	11
D/d_s, Spheres,	3.75	5	6.25	7.5	8.75	10	11.25	12.5	13.75	15	16.25
D/d_{eq}, Cylinders	3.08	4.61	6.15	7.69	9.23	10.76	12.30	13.85	15.38	16.92	18.46
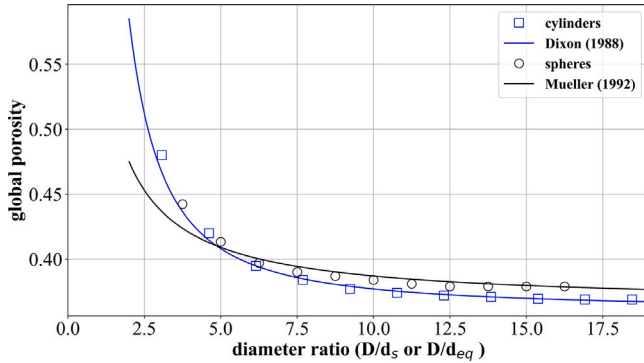
Fig. 7. Global porosity of spheres and cylinders.

is 6.5 mm. Using a length of 100 mm for the cylinders reduces the time required to form the packed bed and the subsequent simulation time. The diameter of the tube D varies from 20 to 260 mm, leading to a range of diameter ratios, as outlined in Table 6, which details the varying D/d_s for spheres and D/d_{eq} for cylinders across different cases.

3.1.2. Evaluation of global porosity

For each generated packed bed, its global porosity ε_g can be calculated as follows:

$$\varepsilon_g = 1 - \frac{V_{solid}}{V_{total}} \quad (6)$$

where V_{solid} and V_{total} represent the volume of particles and the total volume of the packed beds, respectively. To validate the accuracy of the generated packed beds, the global porosity of the listed cases in Table 6 are compared with the classical correlations, which allow to estimate the porosity of packed beds from the diameter ratios. For packed beds with spheres, the Mueller correlation is defined and expressed as follows [27,54]:

$$\varepsilon_g = 0.365 + 0.22/(D/d_s) \quad (7)$$

For cylindrical particles, the Dixon correlation [55] is as follows, applicable when $D/d_{eq} \geq 1.7$:

$$\varepsilon_g = 0.36 + 0.10/(D/d_{eq}) + 0.7/(D/d_{eq})^2 \quad (8)$$

Fig. 7 displays the global porosity of both spherical and cylindrical packed beds as the diameter ratio changes, comparing with the estimates by Mueller and Dixon correlations, respectively. It can be observed that the porosity tends to stabilize as the diameter ratio increases. For spherical particles, the porosity decreases slightly from 0.384 to 0.382 as the diameter ratio increases from 10 (case 6) to 16.25 (case 11) corresponding to a relative decrease of 0.52%. For cylindrical particles, when the diameter ratio changes from 9.23 (case 5) to 18.46 (case 11), the global porosity shifts from 0.372 to 0.370, leading to a relative decrease of 0.53%. These results indicate that the porosity of the packed bed structure remains stable when the diameter ratio is greater than 10.

Furthermore, the simulation results match the empirical values well. Specifically, for spheres, the predicted global porosity is 0.379 at $D/d_s = 12.5$, while the value calculated from the Mueller correlation (Eq. (7)) is 0.382, resulting in a relative error of only 0.7%. These alignments demonstrate the reliability of our simulation approach.

3.1.3. Evaluation of radial porosity

The radial porosity $\varepsilon_A(r)$ is the surface porosity measured at a radial distance r, r ranges from 0 to the radius of the container $R = D/2$. Its definition is given by [32]:

$$\varepsilon_A(r) = \frac{A_{void}(r)}{A(r)} = \frac{A_{void}(r)}{2\pi rL} \quad (9)$$

where $A_{void}(r)$ and $A(r)$ is the void/total area at that radius, respectively. The global porosity ε_g can actually be derived by integrating the radial porosity over r:

$$\varepsilon_g = \frac{V_{void}}{V_{total}} = \frac{\int_0^R \varepsilon_A(r) \cdot 2\pi rL \, dr}{\pi R^2 L} = \frac{\int_0^R \varepsilon_A(r) \cdot 2r \, dr}{R^2} \quad (10)$$

In Mueller's work [27], it was noted that radial porosity exhibits oscillations as a function of distance from the wall, denoted as l, which is dimensionless and calculated as follows:

$$l = \frac{R - r}{d_s} \quad (11)$$

The packed bed was segmented into cylindrical sub-surfaces aligned with the radial direction for analysis, as shown in Fig. 8(a). The void area was quantified using the Integrate Variables feature in ParaView [56]. Fig. 8(b) compares the radial porosity at a diameter ratio of 8.75 between the spherical packed bed and Mueller's experimental results [27]. The radial porosity distribution closely aligns with Mueller's results, replicating both the amplitude and frequency. This confirms the precision of generating packed beds of spheres.

In the previous discussion, it was demonstrated that global porosity remains stable when the diameter ratio is greater than 10. To analyze the effect of diameter ratio on radial porosity, two cases with diameter ratios around 10 were selected. For spheres, the radial porosities of cases 4 and 8 in Table 6 are shown in Fig. 9, with diameter ratios of 7.5 and 12.5, respectively. Similar to Fig. 8, the two curves in Fig. 9 demonstrate a pattern of decaying oscillation. The maximum radial porosity occurs at the wall. As the distance from the wall increases, the amplitude of the oscillations decreases and the width (distance between two troughs) of each oscillation increases, indicating that the spheres are packed more tightly and more uniformly towards the center.

For cylinders, the radial porosities of cases 4 and 8 in Table 6 are shown in Fig. 10, with diameter ratios of 7.69 and 13.85, respectively. Both curves exhibit a consistent oscillation pattern, with a gradual decay in amplitude as the distance from the container wall increases. Unlike the regular oscillations observed in spherical particles, the porosity oscillations of cylindrical particles display greater complexity and irregularity due to their geometric alignment and interactions. The insets provide cut-off views of the bed with a diameter ratio of 13.85 at $l = 0.002, 0.624, 1.296, 1.944, 2.592, 3.24, 3.888, 4.536, 5.184, 5.832,$ and 6.480, offering visualizations of the particle arrangements inside the container.

3.2. Mathematical model and numerical implementation

The 3D domain for computation is presented in Fig. 11, aligned with the structure in experiments as in Fig. 3, consisting of: the inlet, the packed beds, and the outlet section. Flow within these sections is assumed to be incompressible and laminar, as the maximum Reynolds numbers studied are around 708, well below 1240 [57], with isothermal conditions [7,11,31]. The simulations were not extended to higher Reynolds numbers to explore turbulent flow conditions. The classic
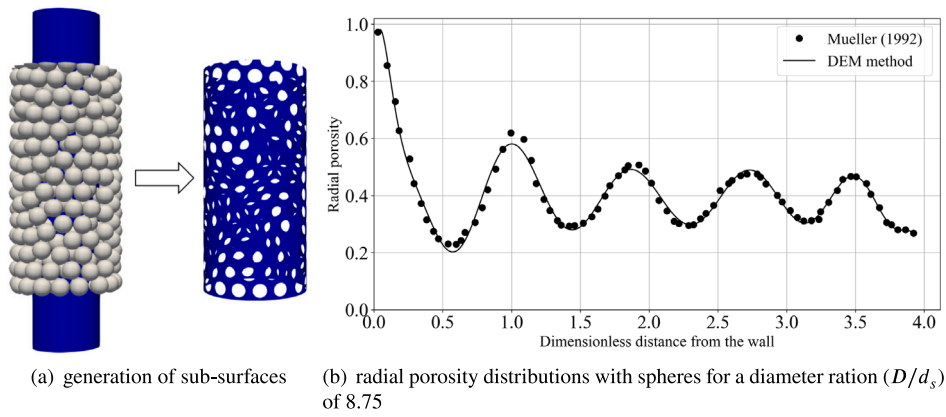
(a) generation of sub-surfaces   (b) radial porosity distributions with spheres for a diameter ration (D/d_s)
                                         of 8.75

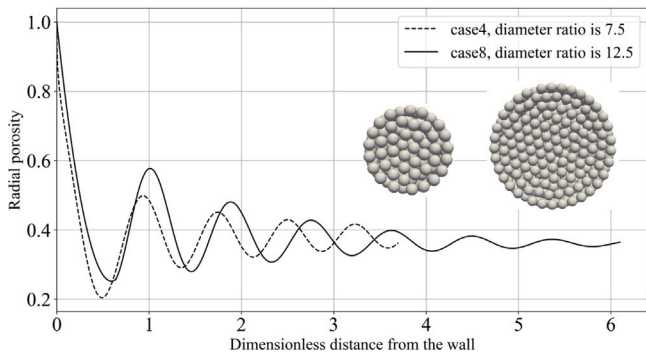**Fig. 8.** Radial porosity distribution and sub-surfaces along the radial direction.

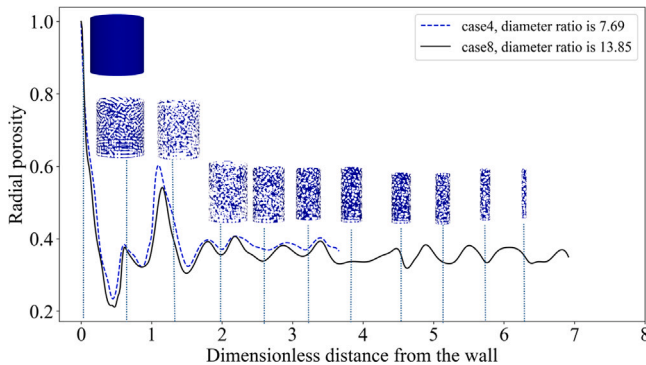**Fig. 9.** Radial porosity distributions of the packed bed spheres with different diameter ratios.

Fig. 10. Radial porosity distributions of the packed bed cylinders with different diameter ratios.

Navier–Stokes equations are employed at the micro-scale, investigating the pressure gradient under steady-state conditions across various geometries, such as spheres or cylinders.

In the simulations, the lengths of L_{in} and L_{out} were set to 50 mm. The sizes of the packed bed for spheres and cylinders were set to $D = 200$ mm, $L = 200$ mm, and $D = 100$ mm, $L = 100$ mm, respectively, because the sphere diameter is 16 mm and the cylinder equivalent diameter is 6.5 mm. This choice ensures a diameter ratio greater than 10, consistent with Fig. 7 showing that the domain is representative of the packed structure considered. Due to computational resources and time constraints, the packed bed in the simulations was not generated at the same size as in the experiments. Instead, the diameter of the bed was kept the same while the length was reduced to save computational time. However, this adjustment is justified as it still produces a stable

Table 7
Boundary conditions for the micro-scale simulation.

Variable	Inlet	Outlet	Walls and fluid-packed bed interface
$\mathbf{v_g}$	$\mathbf{v_g} = (0, 0, v_0)$	$\partial \mathbf{v_g}/\partial \mathbf{n} = \mathbf{0}$	$\mathbf{v_g} = \mathbf{0}$
p	$\partial p/\partial \mathbf{n} = 0$	$p = 0$	$\partial p/\partial \mathbf{n} = 0$

pressure gradient, ensuring the simulation data remains suitable for comparison with experimental results.

3.2.1. Model description

Fluid flows are modeled using Navier–Stokes equations in steady state at the micro-scale, under the assumption of incompressible laminar flow (see Appendix), which are as follows:

$$\begin{cases} \mathbf{v_g} \cdot \nabla \mathbf{v_g} = -\frac{\nabla p}{\rho_g} + \frac{\mu_g \nabla^2 \mathbf{v_g}}{\rho_g} \\ \nabla \cdot \mathbf{v_g} = 0 \end{cases} \tag{12}$$

where $\mathbf{v_g}$ and p represent the velocity and pressure of the fluid, respectively. ρ_g and μ_g denote the density and dynamic viscosity of the fluid.

The boundary conditions for the system in Eq. (12) are provided in Table 7. These boundary conditions have been demonstrated to be the most suitable for non-periodic porous media and have been employed in previous studies for permeability calculations [31]. Air physical properties were evaluated at room temperature (293 K), with density ρ_g is 1.20 kg m^{-3}, dynamic viscosity μ_g of 1.90×10^{-5} kg m^{-1} s^{-1}, and Molar mass M of 28.96 g mol^{-1}, as defined in Table 2 [7].

The numerical model based on the finite volumes method using OpenFOAM [58], was employed to solve Eq. (12). The *pimpleFoam* solver was used, which integrates the pressure-implicit split-operator (PISO) and the semi-implicit method for pressure-linked equations (SIMPLE) algorithms [59,60]. For spatial discretization, second-order schemes with flux limiters were utilized. The convergence criteria for all solutions were set at 10^{-7}.

3.2.2. Evaluation of pressure drop by numerical method

For different particles (spheres and cylinders) within packed beds, the pressure drop was numerically determined by solving the Navier–Stokes equation (Eq. (12)). The analysis of gas flow within the Darcy and Forchheimer regimes required altering the inlet velocity of the gas from 0.00001 to 0.70 m/s, resulting in the Reynolds number increasing from 0.01 to 707.37 for spheres and from 0.004 to 287.37 for cylinders. The range of flow parameters is detailed in Table 8.

The micro-scale simulation was designed to identify the transitional point between the two flow regimes and determine the permeability values K and Forchheimer coefficients β. In the field of porous media, the volume-averaging technique has been proposed for upscaling
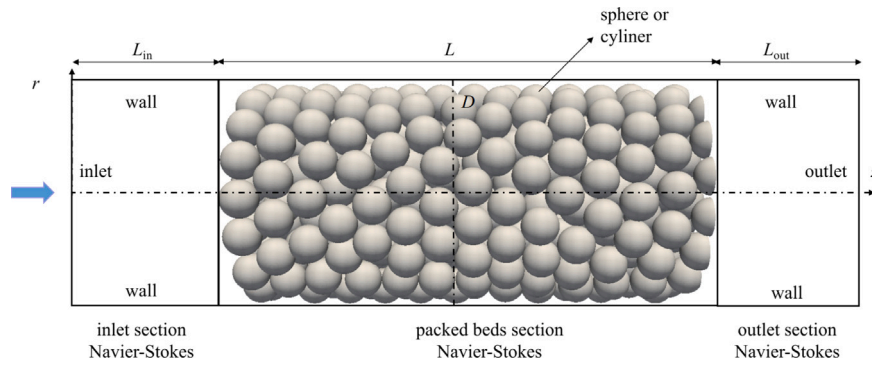
Fig. 11. 3D numerical model of the packed bed.

Table 8
Ranges of flow parameters.

Case	1	2	3	4	5	6	7	8	9	10
Air inlet velocity	0.00001	0.0001	0.001	0.01	0.10	0.20	0.30	0.40	0.50	0.70
Reynolds number, Spheres	0.01	0.10	1.01	10.11	101.05	202.11	303.16	404.21	505.26	707.37
Reynolds number, Cylinders	0.004	0.04	0.41	4.11	41.05	82.11	123.16	164.21	205.26	287.37

micro-scale problems [61]. The pressure gradients ∇p and velocity components $\mathbf{v_g}$, obtained from solving Eq. (12), are subsequently averaged at the macroscopic scale. These averaged values are then substituted into the 1D Darcy–Forchheimer's law, as formulated in Eq. (13).

$$\begin{cases} \nabla \cdot \langle v_g \rangle = 0 \\ \langle v_g \rangle = -\frac{K}{\mu_g} \cdot \left(\frac{\Delta \langle p \rangle^g}{L} + \rho \beta |\langle v_g \rangle|^2 \right) \end{cases} \tag{13}$$

To streamline the presentation and focus solely on the gas phase within the packed beds, the explanation of volume averaging can be revised as follows. In a representative elementary volume (REV) V, the superficial and intrinsic averages of any quantity associated with the gas phase can be distinctly defined. The superficial average of pressure, p, and velocity, v_g, within the gas phase are given by:

$$\langle p \rangle = \frac{1}{V} \int_{V_g} p \, dV, \qquad \langle v_g \rangle = \frac{1}{V} \int_{V_g} \mathbf{v}_g \, dV \tag{14}$$

where V_g is the volume of the gas phase contained within V. The intrinsic phase average, which focuses solely on the volume occupied by the gas phase, is defined for pressure as:

$$\langle p \rangle^g = \frac{1}{V_g} \int_{V_g} p \, dV, \qquad \langle \mathbf{v}_g \rangle^g = \varepsilon_g^{-1} \langle v_g \rangle = \frac{1}{V_g} \int_{V_g} \mathbf{v}_g \, dV \tag{15}$$

The term $\Delta \langle p \rangle^g$ represents the pressure drop within the volume V of the packed beds. Further details about the methodology of volume averaging are extensively discussed in the work of Whitaker et al. [61].

3.2.3. Mesh convergence analysis

The snappyHexMesh utility within the OpenFoam CFD framework [58] was employed to generate a mesh for the fluid domain between the particles. Additionally, adMesh, a software designed for processing triangulated solid meshes [62], was utilized to cover the surface on the right side as depicted in Fig. 12(b). For example, the process of meshing a packed bed filled with spherical particles involves several steps. First, a background mesh is generated, followed by defining both the fluid domain (inlet section, outlet section, and pores within the packed beds section) and the solid domain (particles). The sphere surface is then superimposed onto the background mesh, resulting in a snapped or body-fitted mesh. The final step involves adding layers close to the surfaces, also known as meshing boundary layers. The quality of the resulting mesh is highly contingent on various parameter settings. Once the parameter configuration process is established, the next critical step is to perform a mesh independence verification. This ensures that the final mesh does not unduly influence the simulation results. Fig. 12(a)

displays the refined meshes for spheres in the fluid domain. Details of the meshed geometry of packed beds filled with cylindrical particles are shown in Fig. 13. Lastly, a convergence analysis is necessary to scrutinize the mesh's effect on the final results.

Using the packed bed filled with spherical particles as an example, a mesh convergence study was conducted with pressure and velocity residuals kept below 10^{-7} at the highest inlet velocity (case 10, 0.7 m/s, $Re = 707.37$) due to the presence of the sharpest gradients. The result of the mesh convergence analysis is presented in Fig. 14. The notation ΔP in Fig. 14 represents the average pressure difference between the outlet and inlet,

$$\Delta P = \frac{1}{|A_{g,\text{inlet}}|} \int_{A_{g,\text{inlet}}} p \, ds - \frac{1}{|A_{g,\text{outlet}}|} \int_{A_{g,\text{outlet}}} p \, ds. \tag{16}$$

where $A_{g,\text{inlet}}$ and $A_{g,\text{outlet}}$ denote the cut-off areas of the void spaces at the inlet and outlet of the packed bed, respectively. The relative error δ of pressure drops in two successive meshes in Fig. 14(b) is defined as:

$$\delta = \frac{|\Delta P_{n+1} - \Delta P_n|}{\Delta P_{n+1}} \tag{17}$$

where the index n denotes the simulation with mesh before refinement. The results suggest that when the number of cells exceeds 11.1 million, the error decreases to around 8.4×10^{-3}. Therefore, 11.1 million cells are acceptable for the numerical simulations. Similarly, a mesh convergence test was performed on the packed bed with cylindrical particles at the highest inlet velocity (case 10, 0.7 m/s, $Re = 287.37$). The results are presented in Fig. 15, which indicate that when the number of cells surpass 6.5 million, the error continues to gradually decrease below 7.5×10^{-3} on a logarithmic scale (Fig. 15(b)). Thus, a mesh size of 6.5 million cells is sufficient for simulations involving cylindrical particles.

4. Results comparison and discussion

In the preceding section, experimental measurements of pressure drop in the Forchheimer flow regime were conducted when fluid flows through packed beds. This allowed us to determine values for permeability K and the Forchheimer coefficient β. This section aims to analyze the pertinent parameters through microscopic simulation. Consistency between experimental packing and simulation was maintained by using identical material parameters (glass for spheres, wood for cylinders), emphasizing porosity comparison, and setting the bed diameter to over 10 times the particle size to minimize wall effects. In future work, X-ray images of packed bed structures could be used for
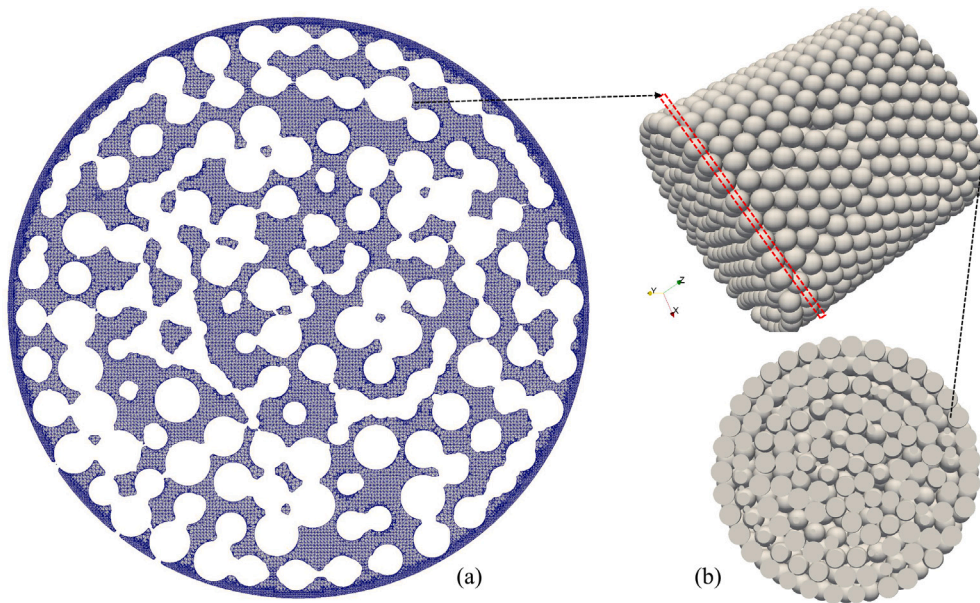
Fig. 12. Mesh of the fluid domain in spheres: (a) mesh displayed on a cross-section, (b) schematic representation of the model's end part.
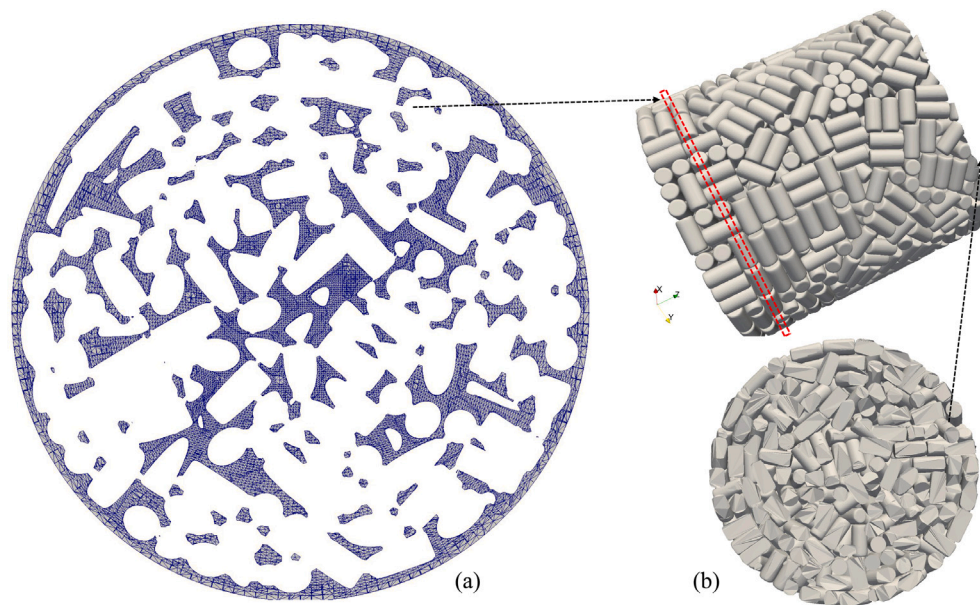

Fig. 13. Mesh of the fluid domain in cylinders: (a) mesh displayed on a cross-section, (b) schematic representation of the model's end part.
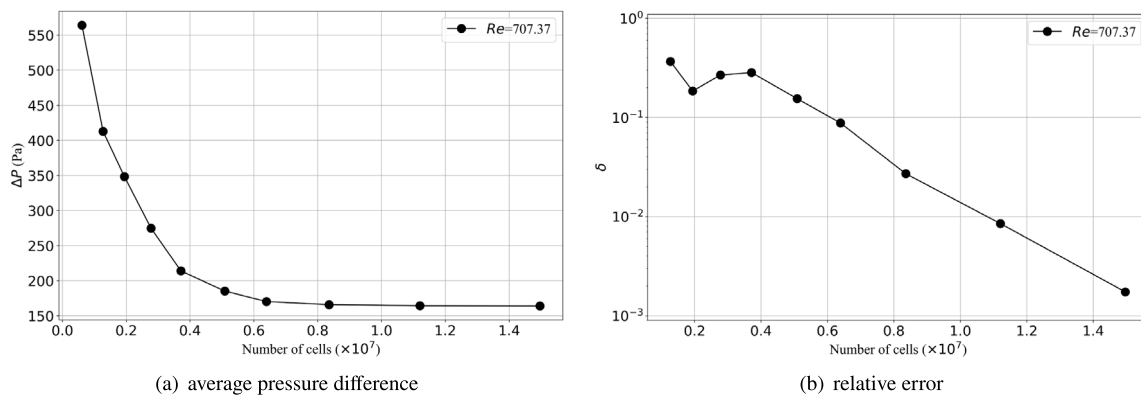

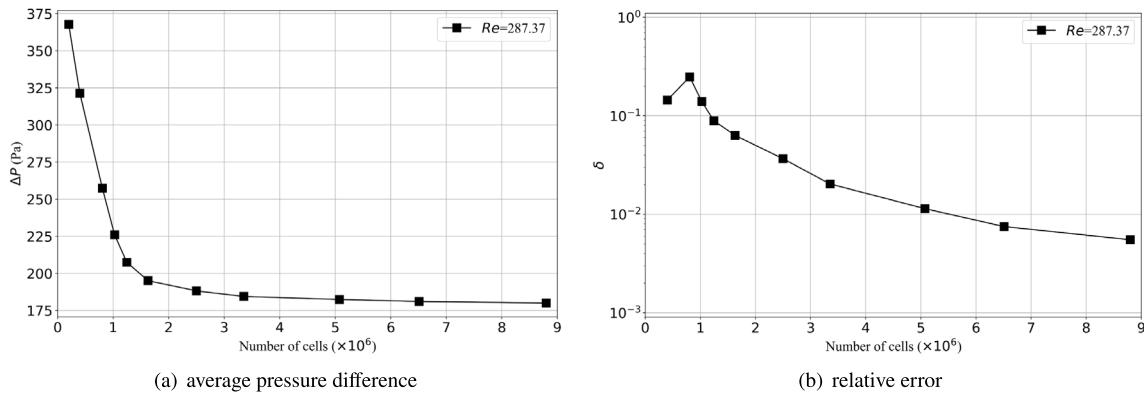**Fig. 14.** Mesh convergence analysis of the fluid domain filled with spheres.

(a) average pressure difference

(b) relative error

Fig. 15. Mesh convergence analysis of the fluid domain filled with cylinders.

Table 9
Permeability K and Forchheimer coefficient β obtained from numerical results.

Particles	Permeability, K (m^2)	Forchheimer coefficient, β (m^{-1})	Limit of Re
Glass spheres	2.59×10^{-7}	1.19×10^3	10.1
Wood pellets	8.49×10^{-8}	2.73×10^3	4.1

simulations and compared with DEM-generated structures to better assess the accuracy of the DEM method. In the first subsection, the values of K and β, as well as the critical Reynolds number for the Darcy flow regime, were obtained from numerical simulations and compared with experimental and correlation results. The second subsection presents a detailed analysis of the flow behavior within packed beds, including streamlines and vorticity.

4.1. Determination of K and β

4.1.1. Numerical results

Fig. 16 presents a comparison between the measured and predicted results for glass spheres, with the measured results shown as red dots and the predicted results, obtained by solving the Navier–Stokes equations (Eq. (12)) and the macroscopic scale equations (Eq. (13)), represented by a dashed line. In Fig. 16(a) and (b), the y-axis shows the intrinsic average pressure gradient, and in Fig. 16(c) and (d), it represents the effective permeability, as defined in Eq. (5). Fig. 16(b) is a zoomed-in view of the pressure gradient data in (a). Similarly, Fig. 16(d) is a zoomed-in view of the effective permeability data in (c).

The pressure gradient exhibits a non-linear relationship, encompassing both Darcy and Forchheimer flow regimes, as shown in Fig. 16(a). This is supported by Fig. 16(c), where the constant K_{eff} at low Re corresponds to the Darcy flow regime. Instead, for Re less than 10.1, the pressure gradient increases linearly, and the effective permeability K_{eff} remains constant, indicating a Darcy flow regime. For Re higher than 10.1, the pressure gradient increases nonlinearly due to inertial effects. In Fig. 16(b), the shaded area represents a $\pm 10\%$ deviation from the experimental data. To obtain the values of K and β, Eq. (4) was used to fit the relationship between $\nabla \langle p_g \rangle^g$ and Re.

For packed beds of wood pellets, as shown in Fig. 17(a), the pressure gradient increases linearly for Re below 4.1 and shows a quadratic dependency beyond this point. This pattern is further compared with the experimental data from Section 2, as presented in the four subfigures of Fig. 17.

The values for both K and β obtained from numerical results are presented in Table 9. The table shows that wood pellets have lower K and a higher β compared to glass spheres, indicating greater resistance to fluid flow. The Reynolds number limit is lower for wood pellets, suggesting the transition to non-linear flow occurs at a lower Reynolds number than for glass spheres.

4.1.2. Comparisons with available correlations

Numerous correlations for predicting pressure drops in packed beds of spheres or cylinders are documented in the literature, with the most suitable ones for this study presented in Table 10, as supported by literature reviews and DEM-CFD results [22,63–66].

In Table 10, pressure drops in packed beds of spheres are evaluated using the Ergun [63] and Reichelt [64] correlations. Unlike Ergun, Reichelt includes wall correction, as referenced by Pavlišič et al. [66]. For cylindrical beds, the comparison is between the Nemec et al. correlation [65], which does not consider wall correction, and the Yazdanpanah et al. correlation [22], which incorporates it and is derived from experimental data. V_c and S are the volume and surface area of each particle. The porosity ε_g is calculated using the correlations defined in Eqs. (7) and (8). K and β were obtained for both types of packed bed materials using experimental methods, numerical simulations, and correlation calculations. To evaluate the differences between these values, the following relative error η is defined

$$\eta = \frac{|i_{exp} - i_{sim/cor}|}{i_{exp}} \tag{18}$$

where i_{exp} is the reference value representing the experimental results, and $i_{sim/cor}$ represents the simulation or correlation results, with i being either K or β. Gravity was neglected in these analyses, and both K and β were treated as scalars.

The comparison of experimental results, simulations, and empirical correlations is presented in Fig. 18, where exp, sim, and cor signify experimental, simulation, and correlation outcomes, respectively. Specifically, cor1 and cor2 denote the first and second correlations from Table 10, which correspond to models without and with wall correction, respectively. For glass spheres, the simulation results for permeability K and the Forchheimer coefficient β closely match the experimental data, showing deviations of 12.20% and 2.46%, respectively. The first correlation, based on Ergun's formula (cor1, glass), reported errors of 14.58% for K and 1.64% for β. Conversely, the second correlation, Reichelt's formula (cor2, glass) which incorporates wall correction, displayed errors of 0.34% for K and 19.67% for β. Reichelt's formula accurately predicts K (with an error of only 0.34%) but shows a larger discrepancy for β. This indicates that including wall corrections more realistically represents pressure drops at lower Reynolds numbers within the Darcy flow regime. However, at higher Reynolds numbers, Reichelt's formula tends to underestimate inertia forces, resulting in larger errors [66]. Considering that the maximum deviation between the simulation results and both correlations, relative
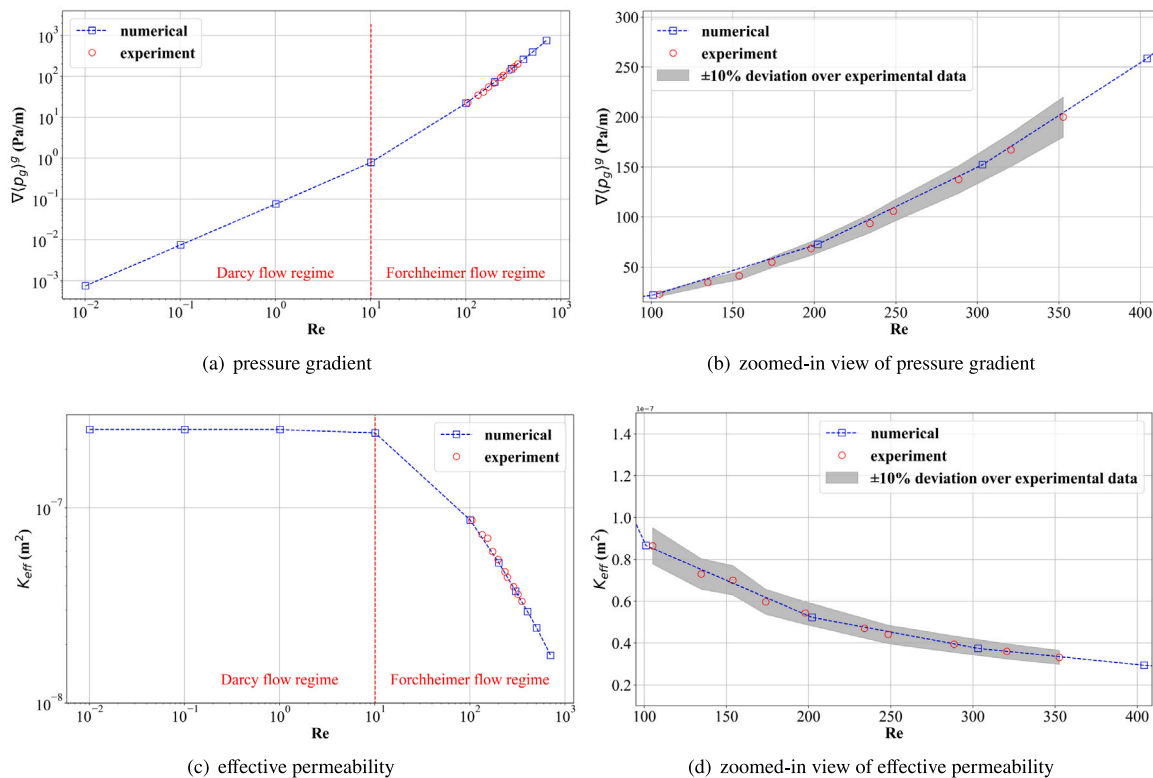
(a) pressure gradient

(b) zoomed-in view of pressure gradient

(c) effective permeability

(d) zoomed-in view of effective permeability

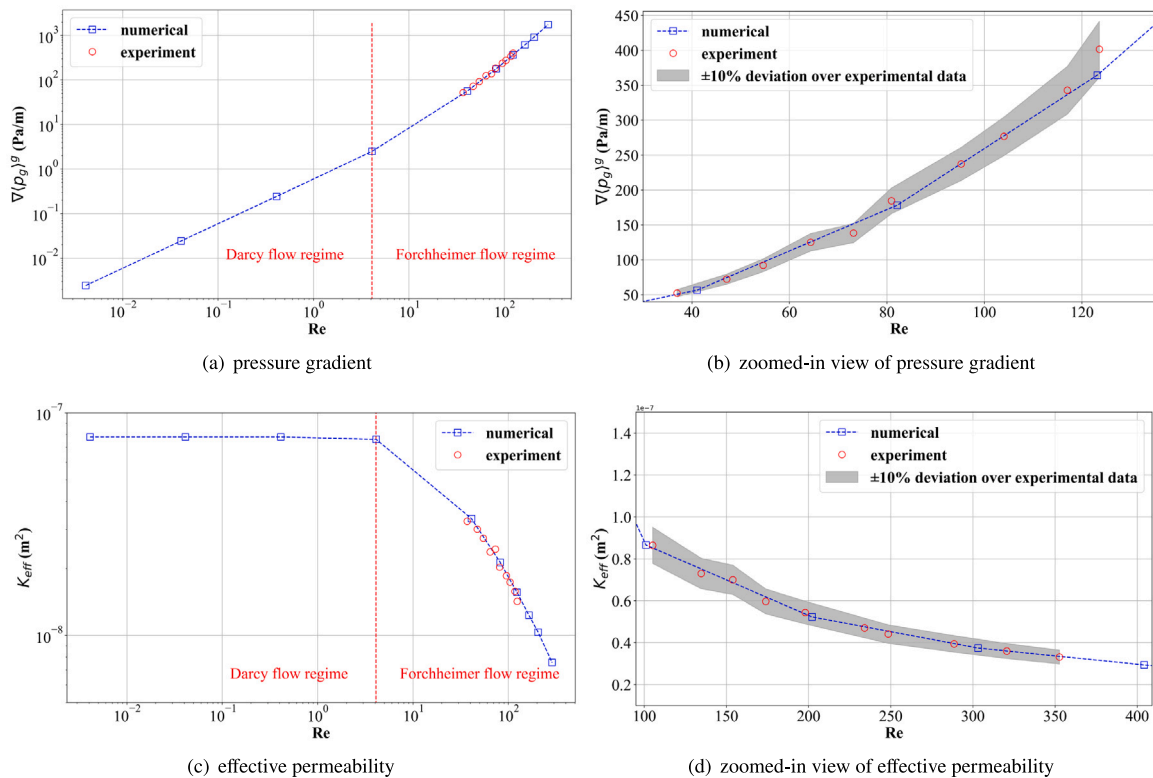**Fig. 16.** Computed pressure gradient and effective permeability with increasing Reynolds number for glass spheres.

(a) pressure gradient

(b) zoomed-in view of pressure gradient

(c) effective permeability

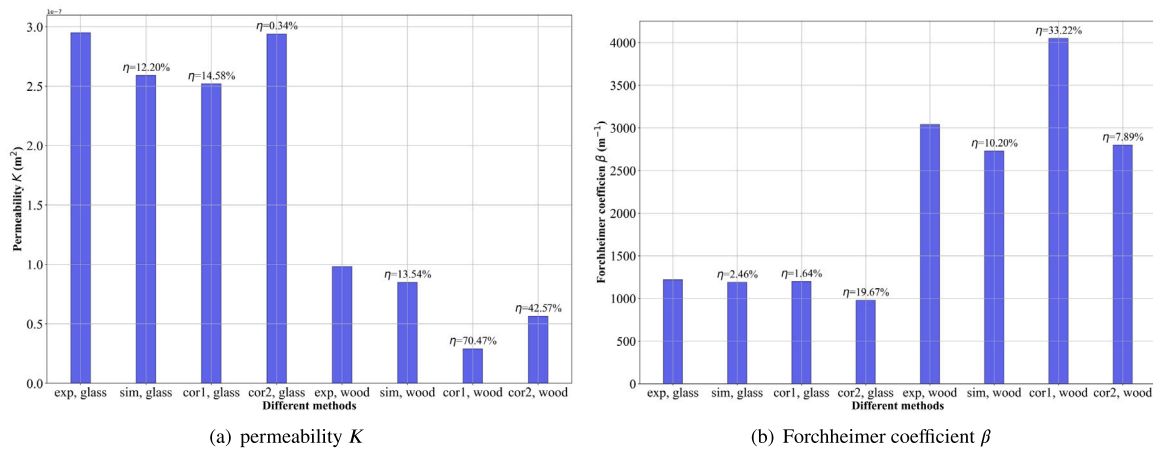(d) zoomed-in view of effective permeability

Fig. 17. Computed pressure gradient and effective permeability with increasing Reynolds number for wood pellets.

Table 10
Correlation equations.

Investigators	Shape of solid inclusions and equation for $\Delta P/L$	Equation for K and β	Wall correction
Ergun (1952) [63]	Sphere $150\frac{(1-\varepsilon_g)^2\mu_g}{\varepsilon_g^3 d_{eq}^2}|\langle v_g\rangle| + 1.75\frac{1-\varepsilon_g}{\varepsilon_g^3 d_{eq}}\rho_g|\langle v_g\rangle|^2$	$K = \frac{\varepsilon_g^3 d_{eq}^2}{150(1-\varepsilon_g)^2}$ $\beta = \frac{1.75(1-\varepsilon_g)}{\varepsilon_g^3 d_{eq}}$	NO
Reichelt (1972) [64]	Sphere $150\frac{(1-\varepsilon_g)^2\mu_g}{\varepsilon_g^3 d_{eq}^2}|\langle v_g\rangle|\cdot\xi^2 + \frac{1-\varepsilon_g}{\varepsilon_g^3 d_{eq}}\rho_g|\langle v_g\rangle|^2\cdot\frac{\xi}{B_W}$ $\xi = 1 + \frac{2}{3(D/d_{eq})(1-\varepsilon_g)}$, $B_W = [1.15(d_{eq}/D)^2 + 0.87]^2$	$K = \frac{\varepsilon_g^3 d_{eq}^2}{150(1-\varepsilon_g)^2}\cdot\xi^2$ $\beta = \frac{1-\varepsilon_g}{\varepsilon_g^3 d_{eq}}\cdot\frac{\xi}{B_W}$	YES
Nemec et al. (2005) [65]	Cylinder $\frac{150}{\Phi^{3/2}}\frac{(1-\varepsilon_g)^2\mu_g}{\varepsilon_g^3 d_{eq}^2}|\langle v_g\rangle| + \frac{1.75}{\Phi^{4/3}}\frac{1-\varepsilon_g}{\varepsilon_g^3 d_{eq}}\rho_g|\langle v_g\rangle|^2$ $\Phi = \pi^{1/3}(6V_c)^{2/3}/S$	$K = \frac{\Phi^{3/2}\varepsilon_g^3 d_{eq}^2}{150(1-\varepsilon_g)}$ $\beta = \frac{1.75(1-\varepsilon_g)}{\Phi^{4/3}\varepsilon_g^3 d_{eq}}$	NO
Yazdanpanah et al. (2011) [22]	Cylinder (wood pellet) $337.11|\langle v_g\rangle| + 3354.26|\langle v_g\rangle|^2$ $4\ mm < l_c < 32\ mm$	$K = \frac{\mu_g}{337.11}$ $\beta = \frac{3354.26}{\rho_g}$	YES

(a) permeability K (b) Forchheimer coefficient β

Fig. 18. Permeability K and Forchheimer coefficient β in packed beds filled with spheres and cylinders: comparison between experimental results and those found by simulation/correlation.

to the experimental values, is less than 20%, it can be concluded that both numerical simulations and empirical correlations are suitable for most practical applications.

For wood pellets, numerical simulations showed lower errors—13.54% for K and 10.20% for β, indicating good predictive accuracy. In contrast, results from empirical correlations indicated higher errors. Specifically, the Nemec et al. correlation (cor1, wood) [65], which does not include wall correction, resulted in errors of 70.47% for K and 33.22% for β. However, the Yazdanpanah et al. correlation (cor2, wood) [22], which accounts for wall correction, reduced errors to 42.57% for K and 7.89% for β. These results suggest that existing correlations may not adequately capture the complex structures of wood pellet-packed beds, leading to lower prediction accuracy compared to numerical simulations, which demonstrated high reliability. The probable reason is that the Nemec et al. correlation attempts to enhance the Ergun equation by incorporating a sphericity factor (Φ), which does not effectively represent the structure of wood pellets. Pavlišič et al. [66] noted that for cylindrical particles, both the sphericity factor and the impact of the specific surface should be considered, as the specific surface affects skin friction drag and subsequently the pressure drop, aspects overlooked by the Nemec et al. correlation. The Yazdanpanah et al. correlation, derived from actual measurements of wood pellets, offers a more accurate and succinct formulation, also considering the wall correction. This correlation reduces the error compared to the Nemec et al. correlation. However, it is specific to wood pellets of certain dimensions (e.g., 6.4 mm in diameter with lengths varying from 4 to 34 mm). Variations in size may affect porosity, packing structure, and the tortuosity of the packed bed, subsequently influencing flow characteristics. Compared to these correlations, our simulation results

showed lower errors. This is due to the DEM method, which employs cylindrical particles that match the exact dimensions of the experimental wood pellets, thus more accurately representing the actual structure. Furthermore, the same physical properties as those used in the experiments are adopted, including factors such as the coefficient of friction and wall corrections. Smaller differences between the simulation results and the experimental data highlight the efficacy of the bed generation and simulation method in capturing the morphological effects on fluid pathways, including tortuosity and the smallest cross-sections along the flow paths.

4.2. Visualization of the flow inside packed beds

In Section 4.1, the critical transition Reynolds number from the Darcy to Forchheimer flow regime for packed beds of glass spheres and wood pellets were determined to be 10.1 and 4.1, respectively, based on the behavior of the pressure gradients as a function of velocity. This subsection aims to visually substantiate these transitions by examining the fluid flow within the packed beds.

4.2.1. Packed bed of glass spheres

As shown in Fig. 19, a cube measuring 50 mm³ was extracted from the entire packed bed structure. This cube is represented in dark gray. Within this cube, the streamlines of the fluid domain are displayed. The streamlines are colored based on velocity magnitude. The YZ plane (X=-0.025 m) was selected to analyze the microscopic behavior of the fluid more clearly.

Fig. 20 shows streamlines within the selected areas at different Reynolds numbers Re = 0.1, 1.0, 10.1, and 50.5. Fig. 20(a), (b), and (c)
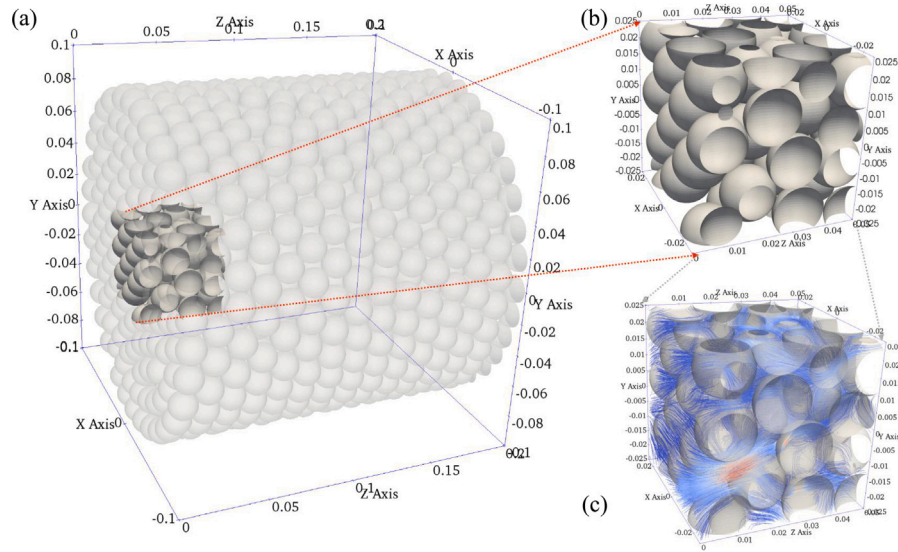
Fig. 19. Schematic location of the analyzed area in the packed beds of glass spheres: (a) location of the selected cube within the entire packed bed, (b) structure of the selected cube, (c) streamlines within the cube represented by velocity magnitude.
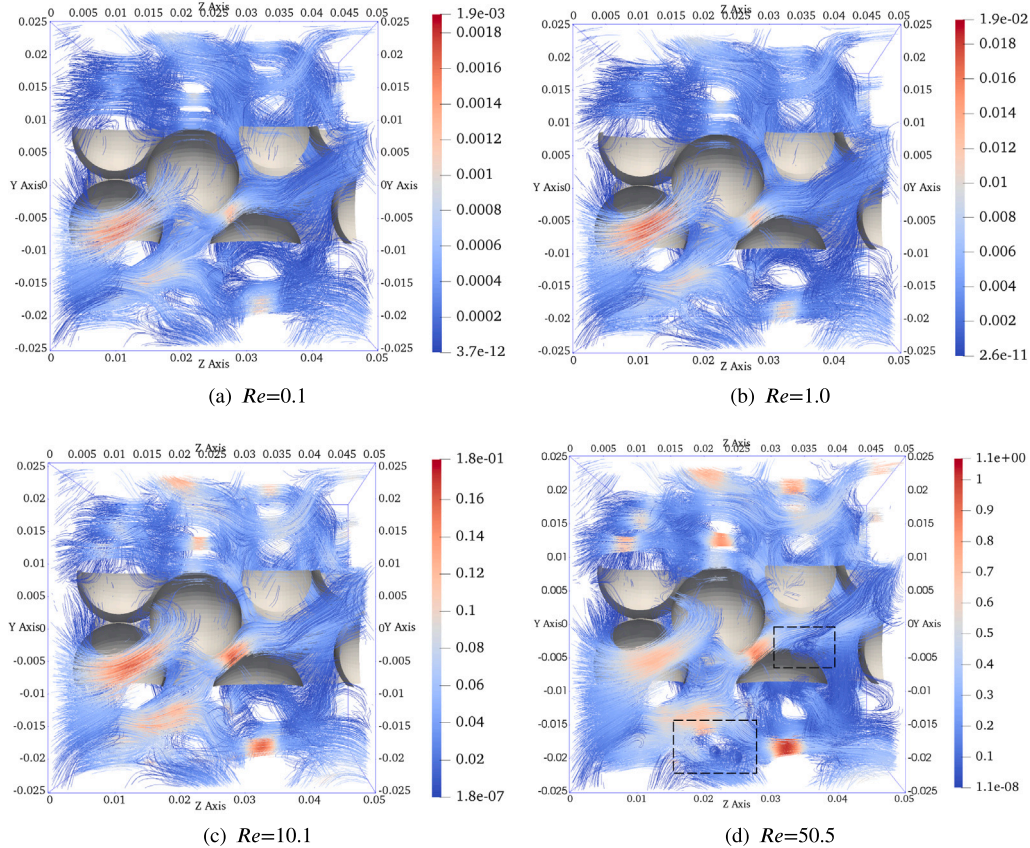

Fig. 20. Streamlines visualization in the packed beds of glass spheres with different Reynolds numbers.

represent velocity streamlines that are nearly the same in distribution, differing only in magnitude. However, at $Re = 50.5$ (Fig. 20(d)), some unique vortices form, highlighted by black text boxes, likely due to non-linear effects. These visualizations demonstrate that as Reynolds numbers increase, fluid flow transitions from Darcy flow to Forchheimer flow (high-vorticity flow).

To study vortices more closely, the analysis is expanded to cover streamlines at Reynolds numbers $Re = 10.1$ and $Re = 50.5$ across the whole packed bed. The results are shown in Fig. 21. With the increase

in Reynolds number, five vortices were found in areas outlined by black dashed lines (see Fig. 21 b). These vortices mostly appeared where several particles touch each other. This suggests that vortices form more often in areas where particles meet.

Next, we compute the vorticity based on the simulated flow velocity. The vorticity vector ω, which describes the tendency of a flow to rotate, is defined as [67]

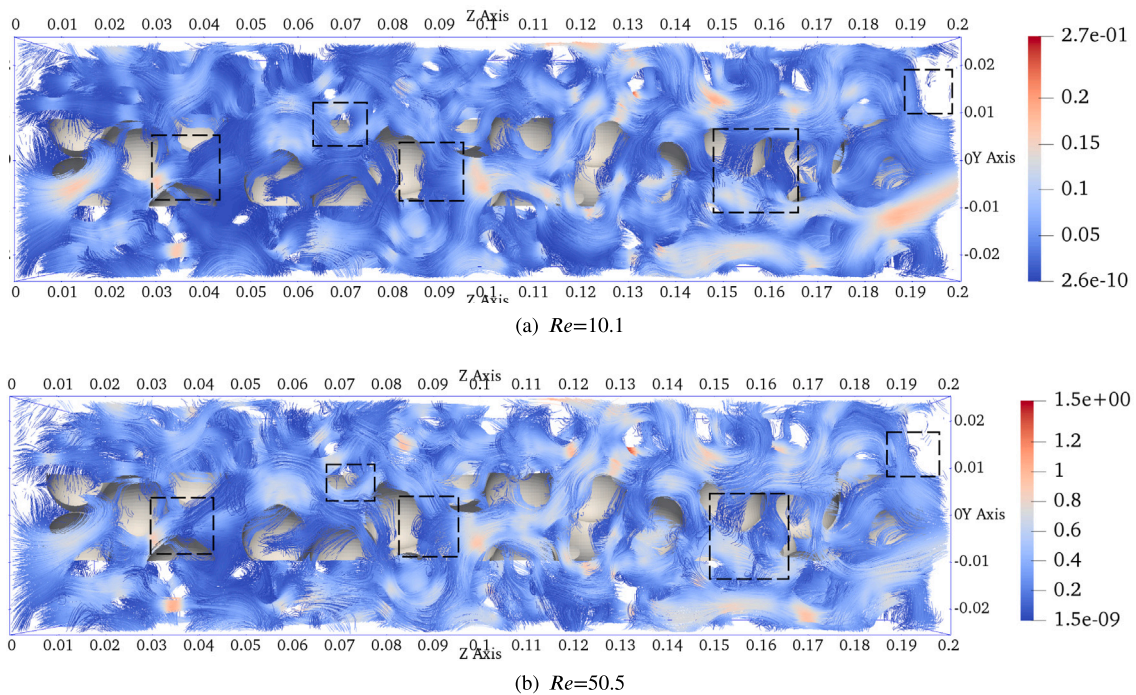$$\omega = \nabla \times v_g \tag{19}$$

(a) $Re=10.1$

(b) $Re=50.5$

Fig. 21. The comparison of streamlines at two different Reynolds numbers.

Table 11
Mean vorticity variation as a function of different Reynolds numbers.

Re	0.1	1.0	10.1	50.5
$|\omega^*|$	0.8117	0.8117	0.8100	0.7793
$\Delta|\omega^*|$	/	0.00%	0.209%	3.992%

For an incompressible flow, this field is governed by the following equation [67].

$$\frac{\partial \boldsymbol{\omega}}{\partial t} + (\boldsymbol{v_g} \cdot \nabla)\boldsymbol{\omega} = (\boldsymbol{\omega} \cdot \nabla)\boldsymbol{v_g} + \nu\nabla^2\boldsymbol{\omega} \qquad (20)$$

Vorticity rises proportionally with velocity in the Darcy flow regime because of its linear behavior and a constant source term. However, this trend changes when transitioning from Darcy to Forchheimer flow due to the velocity field's nonlinear traits. Therefore, calculating the average vorticity across the region is an effective way to assess Darcy flow validity. The linear dependence on velocity is calculated by using the dimensionless vorticity defined as:

$$\omega^* = \frac{\omega}{Re} \frac{\rho_g d_s^2}{\mu_g} \qquad (21)$$

This value should remain constant in the Darcy flow regime. Table 11 shows results for packed beds of glass spheres at different Reynolds numbers, presenting mean vorticity across the analyzed area (Fig. 19), where the $\Delta|\omega^*|$ represents the difference compared to the lowest Reynolds number case. The data in Table 11 show that vorticity begins to change at $Re = 10.1$, with a significant shift observed as the Reynolds number increases from 10.1 to 50.5. Therefore, the Darcy flow regime limit could be set at $Re = 10.1$.

The streamline visualization in packed beds, colored by vorticity magnitude at different Reynolds numbers, is presented in Fig. 22. Fig. 22(a) shows streamlines with particle structure, aimed at demonstrating the impact of packed bed particles on fluid rotation and vortex features. Fig. 22(b) and (c) display streamlines at $Re = 10.1$ and 50.5, respectively. Colored arrows are used to represent the vorticity vectors. The length and color of the arrows indicate the magnitude of vorticity, while their direction shows the orientation of vorticity. The color transition from blue (lower vorticity) to red (higher vorticity) indicates an

increase in vorticity, and the length of the arrows provides visual clues about the magnitude of vorticity. A distribution of vortices is observed in Fig. 22(c), characterized by the clustering of arrow directions in local areas, indicating intense rotational motion of the fluid in these spots. The distribution of vorticity allows for a better understanding of the fluid flow structure throughout the region, particularly near porous media or obstacles where complex vortex structures are commonly formed.

4.2.2. Packed bed of wood pellets

The arrangement of wood pellets in the packing, characterized by complex contact angles, results in intricate streamline patterns within the packed beds, as shown in Fig. 23. The gas streamlines within the selected area (with dimensions of 30 mm in length, 30 mm in width, and 50 mm in height) are analyzed.

Fig. 24 displays streamlined visualization in wood pellet packed beds at different Reynolds numbers. Compared to glass spheres, the streamlines in wood pellet beds are more chaotic and irregular, indicating more unstable fluid flow. At lower Reynolds numbers ($Re = 0.04$, 0.41, 4.10), the streamline distribution remains nearly unchanged, with only changes in velocity values. In contrast, at higher Reynolds numbers ($Re = 20.50$), vortices appear in the regions marked by black dashed lines. Although the vortices are not so obvious, the high-velocity regions (bright streamlines, velocity from 0.25 to 0.48 m/s) at high Re are more extensive than those at lower Re. The analysis of flow visualization within the packed beds concludes that it presents the transition from Darcy to Forchheimer flow from the perspective of the internal flow field.

To observe variations in vortices along the entire length of the packed bed, streamlines were extended across the entire bed. Fig. 25 presents the streamlines at two higher Reynolds numbers ($Re = 4.01$ and 20.50). In Fig. 25(b), obvious vortices are not visible. At the lower Re ($Re = 4.01$), the velocity distribution ranges from 0.01 to 0.089 m/s, with more low-velocity regions (blue streamlines, 0.01 to 0.04 m/s). At the higher Re ($Re = 20.50$), the velocity distribution expands from 0.01 to 0.45 m/s, indicating a broader range of speeds. High-velocity regions (bright streamlines, 0.25 to 0.45 m/s), such as in the lower-left corner of Fig. 25(b), are more prominent.
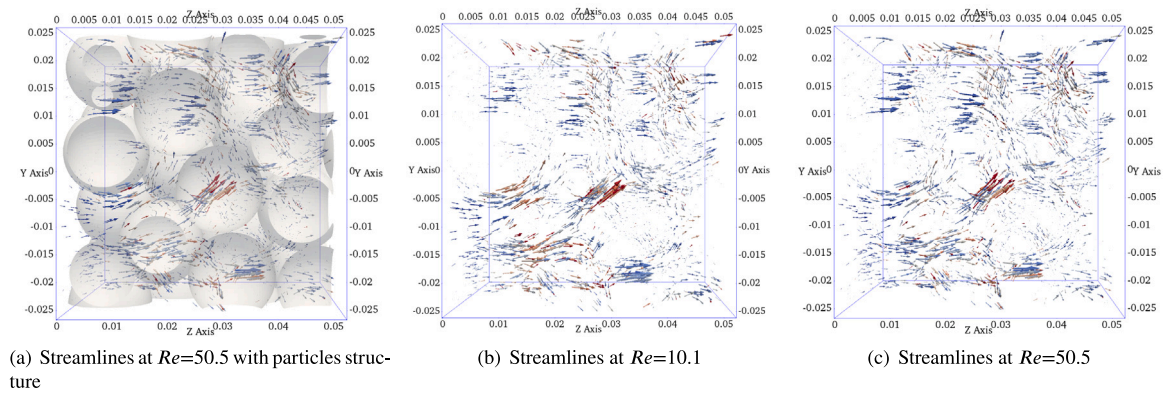
(a) Streamlines at *Re*=50.5 with particles structure   (b) Streamlines at *Re*=10.1   (c) Streamlines at *Re*=50.5

Fig. 22. Streamlines visualization in packed beds: colored by vorticity magnitude at different Reynolds numbers. (For interpretation of the references to colour in this figure legend, the reader is referred to the web version of this article.)
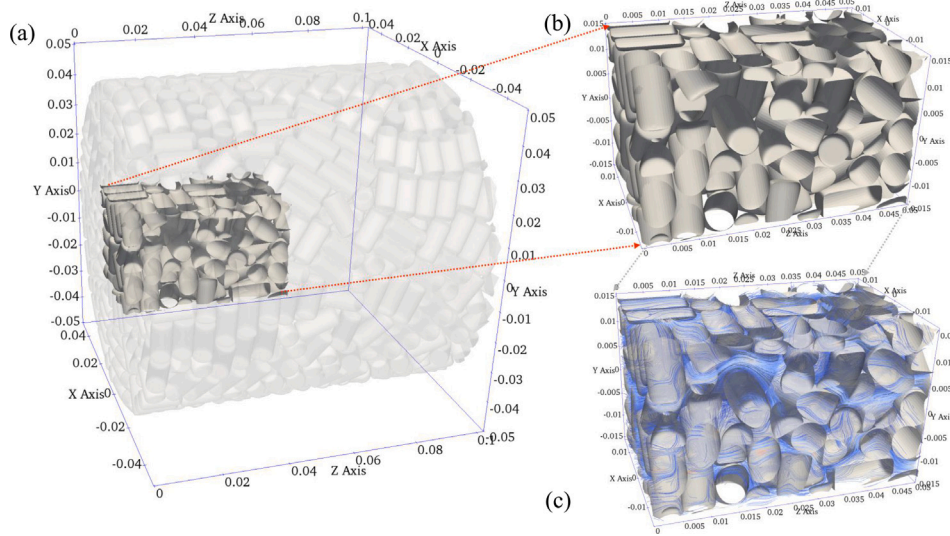

Fig. 23. Schematic location of the analyzed area in the packed beds of wood pellets: (a) location of the selected area within the entire packed bed, (b) structure of the selected area, (c) streamlines within the area represented by velocity magnitude.

Table 12
Mean vorticity variation as a function of different Reynolds numbers in wood pellet packed beds.

Re	0.04	0.41	4.01	20.50
$|\omega^*|$	0.1043	0.1043	0.1038	0.0899
$\Delta|\omega^*|$	/	0.00%	0.479%	13.81%

Similarly, the dimensionless parameter, mean vorticity variation, denotes shifts in the fluid flow regime. As shown in Table 12, the alteration in $\Delta|\omega^*|$ from $Re = 0.41$ to 4.01 is negligible, about 0.479%. In contrast, the transition from $Re = 4.01$ to 20.50 exhibits a notable increase of about 13.81%. This substantial variation exceeds the changes observed when moving from Darcy to Forchheimer flow regimes ($Re = 10.1$, $\Delta|\omega^*| = 3.992\%$) with glass sphere particles, attributed to the complex structure created by the cylindrical stacking of wood pellets. The limit for the Darcy flow regime could feasibly be established at $Re = 4.01$, subject to the required level of precision.

Fig. 26 shows the streamline visualization in packed beds of cylindrical wood pellets, differentiated by vorticity magnitude at differing Reynolds numbers. Specifically, Fig. 26(a) displays the cylindrical wood pellets' streamlines and structural layout. The streamlines, which wrap around the particles, enhance the visibility of how particles affect fluid flow. Figs. 26 (b) and (c) show streamlines at Reynolds numbers of 4.01 and 20.05. In these figures, the colors and arrows on the streamlines

represent the vorticity's magnitude and direction. The color gradient shifts from blue to red, indicating an increase in vorticity which reflects the fluid's rotation near the particles. Larger red arrows point to areas with higher vorticity, typically seen where fluid velocity undergoes significant changes.

5. Conclusions

The objective of this work was to identify the validity domain of the Darcy vs Forchheimer flow regime in terms of a critical Reynolds number, determine macroscopic properties such as permeability K and the Forchheimer coefficient β, and obtain structural parameters like porosity and radial porosity of particles within the packed bed through experimental and DEM-generated structure-based characterization. An experimental setup was designed to measure the pressure drop and flow rates across packed beds. Experiments were conducted using air, with Reynolds numbers ranging from 28.3 to 455.7 for glass spheres and 11.5 to 185.1 for wood pellets, covering the Forchheimer flow regimes. Two 3D randomly packed beds filled with particles of the same shape and material properties as those used in the experiments were generated via the DEM software LIGGGHTS. Structural parameters like porosity and radial porosity, which are not easy to measure directly through experiments, were analyzed. The incompressible Navier–Stokes equations were solved for both Darcy and Forchheimer flow regimes. The main conclusions drawn from this study are as follows:
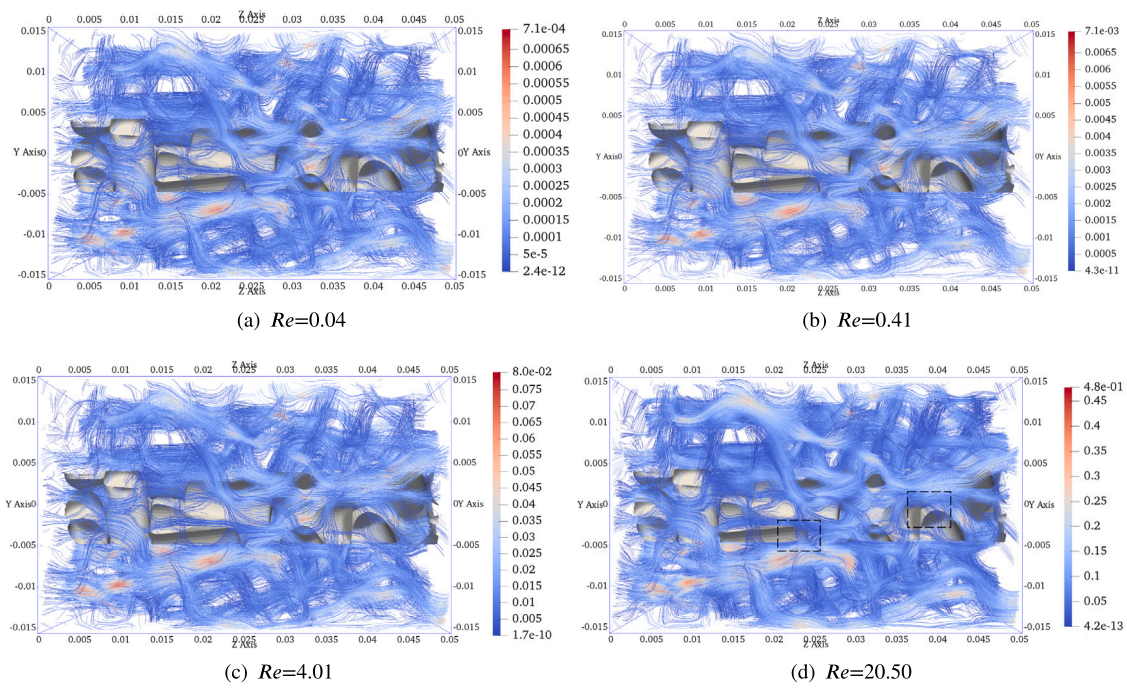
Fig. 24. Streamlines visualization in the packed beds of wood pellets with different Reynolds numbers.
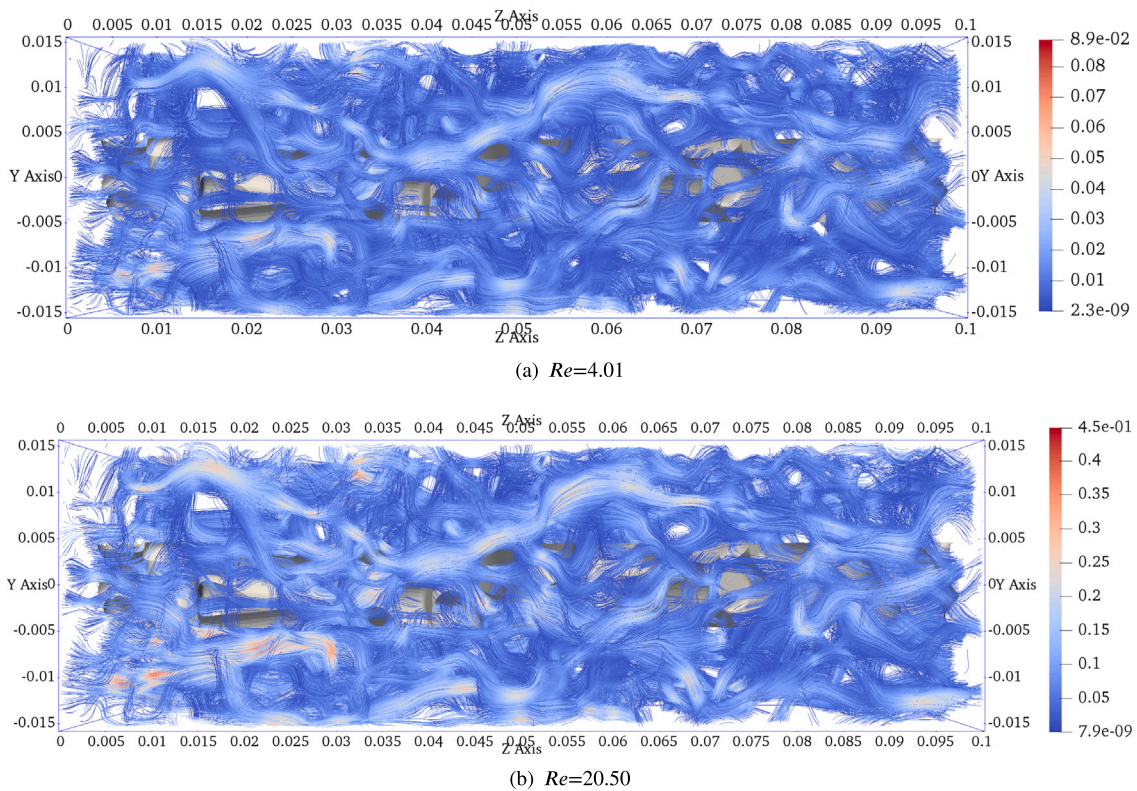

Fig. 25. The comparison of streamlines in the packed beds of wood pellets at two different Reynolds numbers.

(1) It was determined that porosity in packed beds of glass spheres and wood pellets stabilizes beyond diameter ratios of 10 and 9.23, respectively. In beds of glass spheres, radial porosity shows decaying harmonic oscillations across different diameter ratios. In contrast, beds of wood pellets exhibit an irregularly oscillatory radial porosity distribution that stabilizes far from the cylinder wall.

(2) The permeability (K) and Forchheimer coefficient (β) for the packed bed of glass spheres and wood pellets were determined using experimental methods, numerical simulations, and correlations. Experiments showed K values of $2.95 \times 10^{-7} \text{m}^2$ and β values 1.22×10^3 m^{-1} for glass spheres; for wood pellets, K values were 9.82×10^{-8} m^2 and β values 3.04×10^3 m^{-1}. Using experimental results as references,

(a) Streamlines at Re=20.05 with particles   (b) Streamlines at Re=4.01   (c) Streamlines at Re=20.05
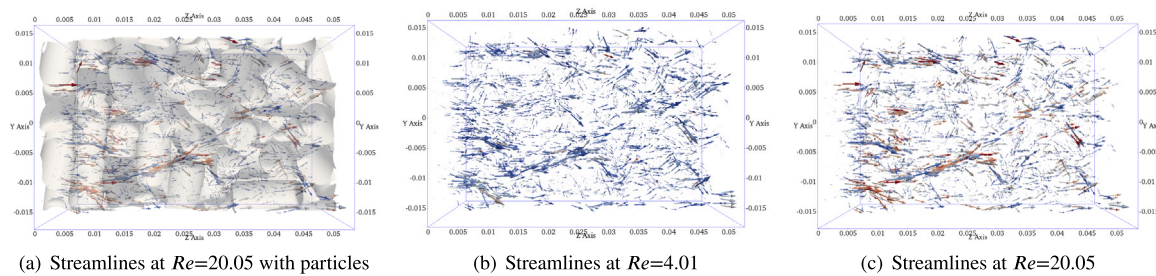
Fig. 26. Streamlines visualization in the packed beds of wood pellets with different Reynolds numbers.

Table 13
Summary of model selection for simulating fluid flow in randomly packed beds.

Investigators	Flow state	Model	Range	Remarks
Gunjal et al. (2005) [68]	laminar	incompressible	Re<2368	analyze pressure drop
Mohanty et al. (2016) [69]	laminar	unsteady-state	Re= 263, 312	analyze pressure drop
Pavlišič et al. (2018) [66]	laminar	steady-state incompressible	$Re>10$	analyze pressure drop
Sassanis et al. (2021) [38]	laminar	steady-state incompressible	7<Re<70	analyze heat transfer
Noël et al. (2022) [70]	laminar	steady-state incompressible	10<Re<100	analyze heat transfer
Noël et al. (2023) [71]	laminar	steady-state incompressible	5<Re<243	analyze pressure drop
Bai et al. (2009) [72]	turbulent	$k-\varepsilon$ model	2000 < Re < 20000	analyze pressure drop
Jiang et al. (2018) [43]	turbulent	LES/RANS, $k-\varepsilon$ model	Re = 9782, 39044	analyze vortex characteristics
Jiang et al. (2018) [44]	turbulent	$k-\varepsilon$ model	Re = 14241, 57012	turbulence characteristics

simulation errors were lower than those from the correlations. For wood pellets, simulation errors were 13.54% for K and 10.20% for β, while correlation errors were 42.57% for K and 7.89% for β. This indicates that simulation results are more reliable than existing correlations for the packed bed of wood pellets.

(3) Microscopic simulations identified the critical transition Reynolds number from Darcy to Forchheimer flow regimes at values of 10.1 for glass spheres and 4.1 for wood pellets, based on pressure gradient behavior vs velocity. Further analysis from the perspective of visualizing flow within packed beds clarified that, when the Reynolds number exceeds these transition points, a vortex forms within the packed bed, indicating non-linear effects.

In summary, the critical Reynolds numbers for transitions from Darcy flow to Forchheimer flow, permeability K, and Forchheimer coefficients β from this study are applicable under ambient temperature, non-reactive, incompressible laminar flow, and when the packed bed to particle diameter ratio exceeds 10 (as shown in Section 3.1). The flow visualization results are relevant for both spherical and cylindrical packed beds, focusing on vortex behavior near the critical Reynolds number. This study also presents a robust methodology: (1) Medium generation: use DEM to generate packed bed structures with various particle shapes and sizes. (2) numerical implementation: apply CFD to solve flow equations, either standalone or coupled with energy equations. (3) Parameter determination: use simulation results to derive key parameters like permeability, Forchheimer coefficient, bed tortuosity, and when coupled with heat transfer, dispersion coefficients, volumetric heat transfer coefficients, and more. The methodologies and results developed in this study can be adapted and applied to a broad range of packed bed systems under similar conditions. Looking ahead, this work can be extended to include other particle shapes and various particle size distributions. Future studies could also explore different flow conditions by extending the analysis to higher Reynolds numbers to investigate turbulence.

CRediT authorship contribution statement

Shaolin Liu: Writing – review & editing, Writing – original draft, Software, Methodology. **Azita Ahmadi-Senichault:** Writing – review & editing, Supervision, Methodology. **Amine Ben-Abdelwahed:** Writing – review & editing, Visualization. **Hui Yao:** Writing – review & editing, Validation, Formal analysis. **Jean Lachaud:** Writing – review & editing, Supervision.

Declaration of competing interest

The authors declare that they have no known competing financial interests or personal relationships that could have appeared to influence the work reported in this paper.

Data availability

Data will be made available on request.

Appendix. Modeling of incompressible laminar flow using Navier–Stokes equations

Table 13 summarizes the model selection for simulating fluid flow in randomly packed beds, categorizing the research into studies on pressure drop, heat transfer, vortex characteristics, and turbulence characteristics. It is observed that at lower Reynolds numbers, as in the work of Gunjal et al. [68], Mohanty et al. [69], Pavlišič et al. [66], Sassanis et al. [38], and Noël et al. [70,71], steady-state incompressible laminar flow problems are solved. For higher Reynolds numbers, particularly in studies focusing on turbulence characteristics, the $k-\varepsilon$ model is predominantly employed to account for turbulent conditions, as seen in the research by Bai et al. [72] and Jiang et al. [43,44].

In the present study, the model employed is based on the assumption of laminar flow, substantiated by both the calculated Reynolds number and a physical assessment of the flow. Calculations indicate a maximum Reynolds number of 707.37 (referenced in Table 8), considerably below the commonly accepted threshold for transitioning to turbulent flow, typically around 1240 [57]. The Reynolds number is defined in Eq. (2). It is presumed that the flow is laminar, and fluid viscosity is treated as constant, aligned with the simplified form of the Navier–Stokes equations presented in Eq. (12).

The objective of this work is to delineate the validity domain of the Darcy versus Forchheimer flow regimes using a critical Reynolds number and to determine macroscopic properties. Laminar flow simulations are utilized accordingly. To address local effects more thoroughly in future studies, it would be advantageous to expand the range of flow to higher Reynolds numbers and to incorporate turbulence models.

References

[1] H. Khodaei, G.H. Yeoh, F. Guzzomi, J. Porteiro, A CFD-based comparative analysis of drying in various single biomass particles, Appl. Therm. Eng. 128 (2018) 1062–1073, http://dx.doi.org/10.1016/j.applthermaleng.2017.09.070.

[2] C. Di Blasi, C. Branca, V. Lombardi, P. Ciappa, C. Di Giacomo, Effects of particle size and density on the packed-bed pyrolysis of wood, Energy Fuels 27 (11) (2013) 6781–6791, http://dx.doi.org/10.1021/ef401481j.

[3] H.B. Chekib Ghabi, M. Sassi, Two-dimensional computational modeling and simulation of wood particles pyrolysis in a fixed bed reactor, Combust. Sci. Technol. 180 (5) (2008) 833–853, http://dx.doi.org/10.1080/00102200801894091.

[4] H. Khodaei, Y.M. Al-Abdeli, F. Guzzomi, G.H. Yeoh, An overview of processes and considerations in the modelling of fixed-bed biomass combustion, Energy 88 (2015) 946–972, http://dx.doi.org/10.1016/j.energy.2015.05.099.

[5] F. Augier, F. Idoux, J. Delenne, Numerical simulations of transfer and transport properties inside packed beds of spherical particles, Chem. Eng. Sci. 65 (3) (2010) 1055–1064, http://dx.doi.org/10.1016/j.ces.2009.09.059.

[6] S. Hamel, W. Krumm, Radial voidage variation in fixed beds of fuel wood pellets, Biomass Bioenergy 46 (2012) 203–209, http://dx.doi.org/10.1016/j.biombioe.2012.08.025.

[7] V. Pozzobon, J. Colin, P. Perre, Hydrodynamics of a packed bed of non-spherical polydisperse particles: A fully virtual approach validated by experiments, Chem. Eng. J. 354 (2018) 126–136, http://dx.doi.org/10.1016/j.cej.2018.07.214.

[8] S. Liu, A. Ahmadi-Senichault, C. Levet, J. Lachaud, Development and validation of a local thermal non-equilibrium model for high-temperature thermal energy storage in packed beds, J. Energy Storage 78 (2024) 109957, http://dx.doi.org/10.1016/j.est.2023.109957.

[9] Y. Yang, R. Pan, Y. Wu, Q. Pan, Y. Shuai, A porous media catalyst for waste polyethylene pyrolysis in a continuous feeding reactor, Energy 302 (2024) 131855, http://dx.doi.org/10.1016/j.energy.2024.131855.

[10] L. Chen, A. He, J. Zhao, Q. Kang, Z.-Y. Li, J. Carmeliet, N. Shikazono, W.-Q. Tao, Pore-scale modeling of complex transport phenomena in porous media, Prog. Energy Combust. Sci. 88 (2022) 100968, http://dx.doi.org/10.1016/j.pecs.2021.100968.

[11] S. Liu, A. Ahmadi-Senichault, V. Pozzobon, J. Lachaud, Multi-scale investigation of heat and momentum transfer in packed-bed TES systems up to 800 K, Appl. Energy 366 (2024) 123285, http://dx.doi.org/10.1016/j.apenergy.2024.123285.

[12] M. Prat, Recent advances in pore-scale models for drying of porous media, Chem. Eng. J. 86 (1) (2002) 153–164, http://dx.doi.org/10.1016/S1385-8947(01)00283-2.

[13] A. Parmigiani, C. Huber, O. Bachmann, B. Chopard, Pore-scale mass and reactant transport in multiphase porous media flows, J. Fluid Mech. 686 (2011) 40–76, http://dx.doi.org/10.1017/jfm.2011.268.

[14] M. Quintard, M. Kaviany, S. Whitaker, Two-medium treatment of heat transfer in porous media: numerical results for effective properties, Adv. Water Resour. 20 (2) (1997) 77–94, http://dx.doi.org/10.1016/S0309-1708(96)00024-3.

[15] R. Pan, Y. Wu, B. Guene Lougou, Y. Shuai, G. Debenest, Numerical study on waste polyethylene pyrolysis driven by self-sustaining smoldering, Sci. China Technol. Sci. 67 (2) (2024) 627–638, http://dx.doi.org/10.1007/s11431-023-2549-3.

[16] U. Hornung, Homogenization and Porous Media, vol. 6, Springer Science & Business Media, 1997.

[17] S. Whitaker, The Method of Volume Averaging, vol. 13, Springer Science & Business Media, 1998.

[18] Ö. Bağcı, N. Dukhan, M. Özdemir, Flow regimes in packed beds of spheres from pre-Darcy to turbulent, Transp. Porous Media 104 (3) (2014) 501–520, http://dx.doi.org/10.1007/s11242-014-0345-0.

[19] M. Sedghi-Asl, H. Rahimi, Adoption of Manning's equation to 1D non-Darcy flow problems, J. Hydraul. Res. 49 (6) (2011) 814–817, http://dx.doi.org/10.1080/00221686.2011.629911.

[20] Z. Zeng, R. Grigg, A criterion for non-Darcy flow in porous media, Transp. Porous Media 63 (2006) 57–69, http://dx.doi.org/10.1007/s11242-005-2720-3.

[21] P. Kundu, V. Kumar, I.M. Mishra, Experimental and numerical investigation of fluid flow hydrodynamics in porous media: Characterization of pre-Darcy, Darcy and non-Darcy flow regimes, Powder Technol. 303 (2016) 278–291, http://dx.doi.org/10.1016/j.powtec.2016.09.037.

[22] F. Yazdanpanah, S. Sokhansanj, A. Lau, C. Lim, X. Bi, S. Melin, Airflow versus pressure drop for bulk wood pellets, Biomass Bioenergy 35 (5) (2011) 1960–1966, http://dx.doi.org/10.1016/j.biombioe.2011.01.042.

[23] J. von Seckendorff, O. Hinrichsen, Review on the structure of random packed-beds, Can. J. Chem. Eng. 99 (S1) (2021) S703–S733, http://dx.doi.org/10.1002/cjce.23959.

[24] G.E. Mueller, A simple method for determining sphere packed bed radial porosity, Powder Technol. 229 (2012) 90–96, http://dx.doi.org/10.1016/j.powtec.2012.06.013.

[25] L. van der Tempel, G.P. Melis, T. Brandsma, Thermal conductivity of a glass: I. Measurement by the glass–metal contact, Glass Phys. Chem. 26 (6) (2000) 606–611, http://dx.doi.org/10.1023/A:1007164501169.

[26] W. Du, N. Quan, P. Lu, J. Xu, W. Wei, L. Zhang, Experimental and statistical analysis of the void size distribution and pressure drop validations in packed beds, Chem. Eng. Res. Des. 106 (2016) 115–125, http://dx.doi.org/10.1016/j.cherd.2015.11.023.

[27] G.E. Mueller, Radial void fraction distributions in randomly packed fixed beds of uniformly sized spheres in cylindrical containers, Powder Technol. 72 (3) (1992) 269–275, http://dx.doi.org/10.1016/0032-5910(92)80045-X.

[28] R. Balzan, A.L. Sellerio, D. Mari, A. Comment, High-precision MRI reconstruction algorithm for 3D sphere packings, Appl. Magn. Reson. 46 (2015) 633–642, http://dx.doi.org/10.1007/s00723-015-0677-0.

[29] A. Džiugys, A.H. Mahmoudi, E. Misiulis, R. Navakas, G. Skarbalius, Fractal dependence of the packed bed porosity on the particles size distribution, Chaos, Solitons Fractals 159 (2022) 112144, http://dx.doi.org/10.1016/j.chaos.2022.112144.

[30] Z. Wang, A. Afacan, K. Nandakumar, K.T. Chuang, Porosity distribution in random packed columns by gamma ray tomography, Chem. Eng. Process. Process Intensif. 40 (3) (2001) 209–219, http://dx.doi.org/10.1016/S0255-2701(00)00108-2.

[31] H. Scandelli, A. Ahmadi-Senichault, C. Levet, J. Lachaud, Computation of the permeability tensor of non-periodic anisotropic porous media from 3D images, Transp. Porous Media (2022) 1–29, http://dx.doi.org/10.1007/s11242-022-01766-8.

[32] H. Liu, C. Zhao, Effect of radial porosity oscillation on the thermal performance of packed bed latent heat storage, Engineering 7 (4) (2021) 515–525, http://dx.doi.org/10.1016/j.eng.2020.05.020.

[33] D.A. Nield, A. Bejan, et al., Convection in Porous Media, vol. 3, Springer, 2006.

[34] M. Mayerhofer, J. Govaerts, N. Parmentier, H. Jeanmart, L. Helsen, Experimental investigation of pressure drop in packed beds of irregular shaped wood particles, Powder Technol. 205 (1) (2011) 30–35, http://dx.doi.org/10.1016/j.powtec.2010.08.006.

[35] M. Hänchen, S. Brückner, A. Steinfeld, High-temperature thermal storage using a packed bed of rocks – heat transfer analysis and experimental validation, Appl. Therm. Eng. 31 (10) (2011) 1798–1806, http://dx.doi.org/10.1016/j.applthermaleng.2010.10.034.

[36] F. Dorai, C. Moura Teixeira, M. Rolland, E. Climent, M. Marcoux, A. Wachs, Fully resolved simulations of the flow through a packed bed of cylinders: Effect of size distribution, Chem. Eng. Sci. 129 (2015) 180–192, http://dx.doi.org/10.1016/j.ces.2015.01.070.

[37] J.C. Ferguson, F. Panerai, A. Borner, N.N. Mansour, Puma: the porous microstructure analysis software, SoftwareX 7 (2018) 81–87, http://dx.doi.org/10.1016/j.softx.2018.03.001.

[38] V. Sassanis, L. Gamet, M. Rolland, R. Ma, V. Pozzobon, Numerical determination of the volumetric heat transfer coefficient in fixed beds of wood chips, Chem. Eng. J. 417 (2021) 128009, http://dx.doi.org/10.1016/j.cej.2020.128009.

[39] N. Dukhan, M.A. Al-Rammahi, A.S. Suleiman, Fluid temperature measurements inside metal foam and comparison to brinkman–Darcy flow convection analysis, Int. J. Heat Mass Transfer 67 (2013) 877–884, http://dx.doi.org/10.1016/j.ijheatmasstransfer.2013.08.055.

[40] A.L. Redman, H. Bailleres, I. Turner, P. Perré, Mass transfer properties (permeability and mass diffusivity) of four Australian hardwood species, BioResources 7 (3) (2012) 3410–3424.

[41] R. Guibert, M. Nazarova, P. Horgue, G. Hamon, P. Creux, G. Debenest, Computational permeability determination from pore-scale imaging: sample size, mesh and method sensitivities, Transp. Porous Media 107 (3) (2015) 641–656, http://dx.doi.org/10.1007/s11242-015-0458-0.

[42] J. Yang, J. Wu, L. Zhou, Q. Wang, Computational study of fluid flow and heat transfer in composite packed beds of spheres with low tube to particle diameter ratio, Nucl. Eng. Des. 300 (2016) 85–96, http://dx.doi.org/10.1016/j.nucengdes.2015.10.030.

[43] J. Linsong, L. Hongsheng, S. Shaoyi, X. Maozhao, W. Dan, B. Minli, Pore-scale simulation of flow and turbulence characteristics in three-dimensional randomly packed beds, Powder Technol. 338 (2018) 197–210, http://dx.doi.org/10.1016/j.powtec.2018.06.013.

[44] J. Linsong, L. Hongsheng, W. Dan, W. Jiansheng, X. Maozhao, Pore-scale simulation of vortex characteristics in randomly packed beds using LES/RANS models, Chem. Eng. Sci. 177 (2018) 431–444, http://dx.doi.org/10.1016/j.ces.2017.11.040.

[45] S. Das, N. Deen, J. Kuipers, Multiscale modeling of fixed-bed reactors with porous (open-cell foam) non-spherical particles: Hydrodynamics, Chem. Eng. J. 334 (2018) 741–759, http://dx.doi.org/10.1016/j.cej.2017.10.047.

[46] E. Erdim, Ö. Akgiray, İ. Demir, A revisit of pressure drop-flow rate correlations for packed beds of spheres, Powder Technol. 283 (2015) 488–504, http://dx.doi.org/10.1016/j.powtec.2015.06.017.

[47] S. Liu, A. Ahmadi-Senichault, H. Scandelli, J. Lachaud, Experimental investigation and tomography analysis of Darcy-Forchheimer flows in thermal protection systems, Acta Astronaut. 218 (2024) 147–162, http://dx.doi.org/10.1016/j.actaastro.2024.02.027.

[48] W. Sobieski, A. Trykozko, Darcy's and Forchheimer's laws in practice. Part 1. The experiment, Tech. Sci./Univ. Warmia Mazury Olsztyn (2014).

[49] S. Liu, A. Ahmadi-Senichault, C. Levet, J. Lachaud, Experimental investigation on the validity of the local thermal equilibrium assumption in ablative-material response models, Aerosp. Sci. Technol. 141 (2023) 108516, http://dx.doi.org/10.1016/j.ast.2023.108516.

[50] C. Kloss, C. Goniva, LIGGGHTS–open source discrete element simulations of granular materials based on lammps, in: Supplemental Proceedings: Materials Fabrication, Properties, Characterization, and Modeling, vol. 2, Wiley Online Library, 2011, pp. 781–788, http://dx.doi.org/10.1002/9781118062142.ch94.

[51] S. Inaba, S. Fujino, K. Morinaga, Young's modulus and compositional parameters of oxide glasses, J. Am. Ceram. Soc. 82 (12) (1999) 3501–3507, http://dx.doi.org/10.1111/j.1151-2916.1999.tb02272.x.

[52] T. Oschmann, H. Kruggel-Emden, Numerical and experimental investigation of the heat transfer of spherical particles in a packed bed with an implicit 3D finite difference approach, Granul. Matter 19 (47) (2017) 1–11, http://dx.doi.org/10.1007/s10035-017-0711-z.

[53] A. Makishima, J.D. Mackenzie, Calculation of bulk modulus, shear modulus and Poisson's ratio of glass, J. Non-Cryst. Solids 17 (2) (1975) 147–157, http://dx.doi.org/10.1016/0022-3093(75)90047-2.

[54] S.S. Halkarni, A. Sridharan, S. Prabhu, Estimation of volumetric heat transfer coefficient in randomly packed beds of uniform sized spheres with water as working medium, Int. J. Therm. Sci. 110 (2016) 340–355, http://dx.doi.org/10.1016/j.ijthermalsci.2016.07.012.

[55] A.G. Dixon, Correlations for wall and particle shape effects on fixed bed bulk voidage, Can. J. Chem. Eng. 66 (5) (1988) 705–708, http://dx.doi.org/10.1002/cjce.5450660501.

[56] J. Ahrens, B. Geveci, C. Law, C. Hansen, C. Johnson, 36-Paraview: An end-user tool for large-data visualization, in: The visualization handbook, vol. 717, Citeseer, 2005, 50038–1.

[57] M.Ö. Çarpinlioğlu, E. Özahi, M.Y. Gündoğdu, Determination of laminar and turbulent flow ranges through vertical packed beds in terms of particle friction factors, Adv. Powder Technol. 20 (6) (2009) 515–520, http://dx.doi.org/10.1016/j.apt.2009.06.006.

[58] H. Jasak, A. Jemcov, Z. Tukovic, et al., Openfoam: A C++ library for complex physics simulations, in: International Workshop on Coupled Methods in Numerical Dynamics, vol. 1000, IUC Dubrovnik Croatia, 2007, pp. 1–20.

[59] H.G. Weller, G. Tabor, H. Jasak, C. Fureby, A tensorial approach to computational continuum mechanics using object-oriented techniques, Comput. Phys. 12 (6) (1998) 620–631, http://dx.doi.org/10.1063/1.168744.

[60] H. Yao, M. Azaiez, C. Xu, New unconditionally stable schemes for the Navier-Stokes equations, Commun. Comput. Phys. 30 (4) (2021) 1083–1117, http://dx.doi.org/10.4208/cicp.OA-2021-0004.

[61] S. Whitaker, The Method of Volume Averaging, vol. 13, Springer Science & Business Media, 2013.

[62] C.J. Conroy, E.J. Kubatko, D.W. West, ADMESH: An advanced, automatic unstructured mesh generator for shallow water models, Ocean Dyn. 62 (10) (2012) 1503–1517, http://dx.doi.org/10.1007/s10236-012-0574-0.

[63] S. Ergun, Fluid flow through packed columns, Chem. Eng. Prog. 48 (2) (1952) 89–94.

[64] W. Reichelt, Zur Berechnung des Druckverlustes einphasig durchströmter Kugel-und Zylinderschüttungen, Chem. Ing. Tech. 44 (18) (1972) 1068–1071, http://dx.doi.org/10.1002/cite.330441806.

[65] D. Nemec, J. Levec, Flow through packed bed reactors: 1. Single-phase flow, Chem. Eng. Sci. 60 (24) (2005) 6947–6957, http://dx.doi.org/10.1016/j.ces.2005.05.068.

[66] A. Pavlišič, R. Ceglar, A. Pohar, B. Likozar, Comparison of computational fluid dynamics (CFD) and pressure drop correlations in laminar flow regime for packed bed reactors and columns, Powder Technol. 328 (2018) 130–139, http://dx.doi.org/10.1016/j.powtec.2018.01.029.

[67] M. Aminpour, S.A. Galindo-Torres, A. Scheuermann, L. Li, Pore-scale behavior of Darcy flow in static and dynamic porous media, Phys. Rev. Appl. 9 (2018) 064025, http://dx.doi.org/10.1103/PhysRevApplied.9.064025.

[68] P.R. Gunjal, V.V. Ranade, R.V. Chaudhari, Computational study of a single-phase flow in packed beds of spheres, AIChE J. 51 (2) (2005) 365–378, http://dx.doi.org/10.1002/aic.10314.

[69] R. Mohanty, S. Mohanty, B. Mishra, Study of flow through a packed bed using discrete element method and computational fluid dynamics, J. Taiwan Inst. Chem. Eng. 63 (2016) 71–80, http://dx.doi.org/10.1016/j.jtice.2016.03.025.

[70] E. Noël, D. Teixeira, New framework for upscaling gas-solid heat transfer in dense packing, Int. J. Heat Mass Transfer 189 (2022) 122745, http://dx.doi.org/10.1016/j.ijheatmasstransfer.2022.122745.

[71] E. Noël, D. Teixeira, G. Preux, Modelling of gas-solid heat transfer and pressure drop in a rock-packed bed using pore-scale simulations, Int. J. Heat Mass Transfer 214 (2023) 124432, http://dx.doi.org/10.1016/j.ijheatmasstransfer.2023.124432.

[72] H. Bai, J. Theuerkauf, P.A. Gillis, P.M. Witt, A coupled DEM and CFD simulation of flow field and pressure drop in fixed bed reactor with randomly packed catalyst particles, Ind. Eng. Chem. Res. 48 (8) (2009) 4060–4074, http://dx.doi.org/10.1021/ie801548h.